ARTICLE

Synthesis and design of manganese and nickel complexes with potential anticancer and antibacterial activities, and antiviral properties for therapeutic applications

Reyaz Ahmad[a], Mukesh Choudhary[a]*

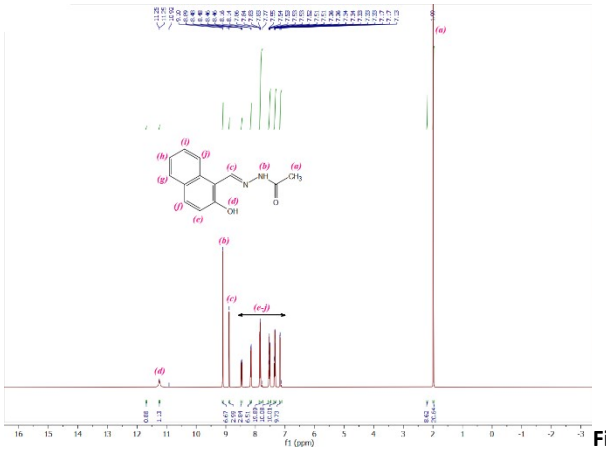

Figure S1. ^{1}H-NMR spectra of Schiff base (SB) ligand in DMSO-d6 solution.

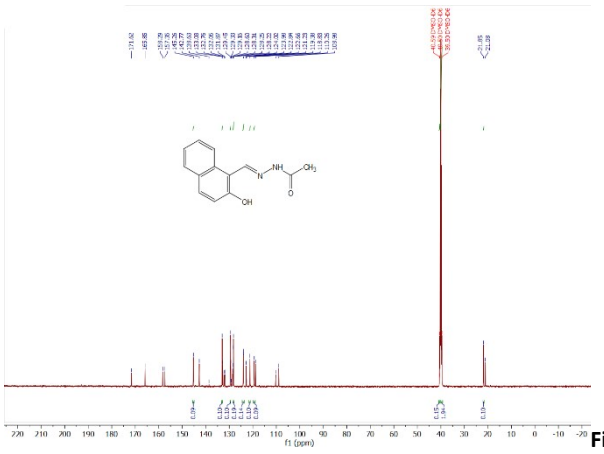

Figure S2. ^{13}C-NMR spectra of Schiff base (SB) ligand in DMSO-d6 solution.

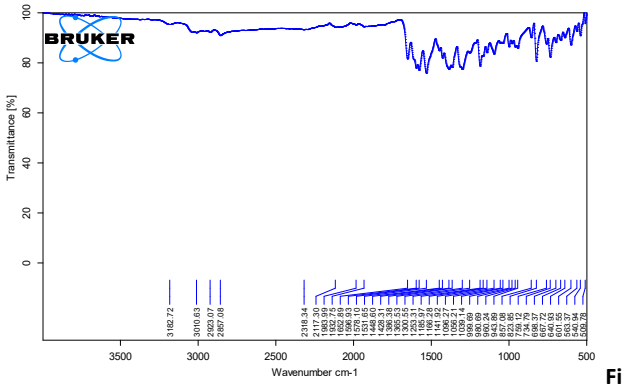

Figure S3. FT-IR spectra of Mn(III) complex (**1**) of Schiff base (SB) ligand.

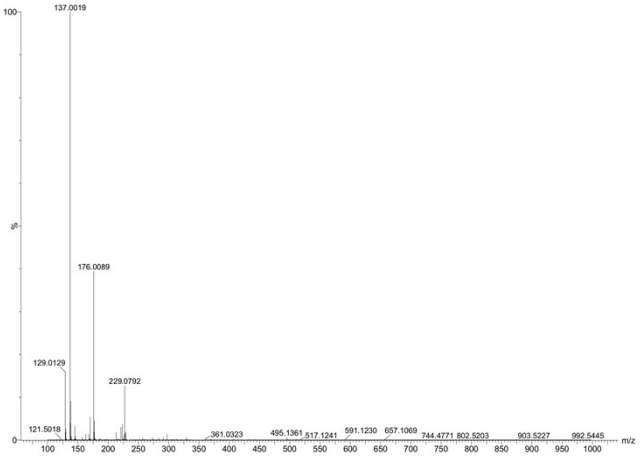

Figure S4. HRMS spectra of Schiff base (SB) ligand.

[a] *Department of Chemical Science and Technology, National Institute of Technology Patna, Patna-800005 (Bihar) India.*

[a.] *Corresponding author: mukesh@nitp.ac.in*

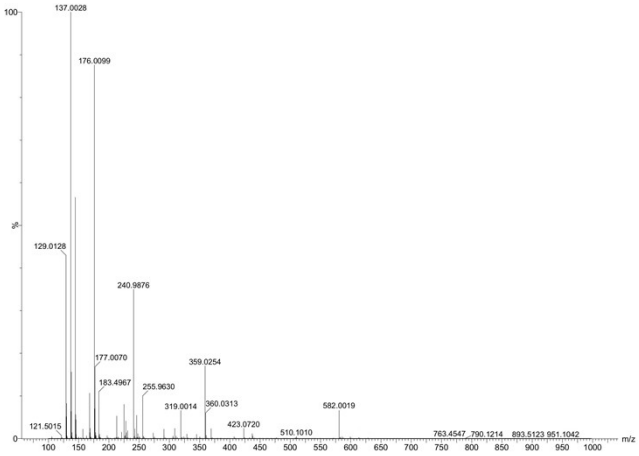

Figure S5. HRMS spectra of Mn(III) complex (**1**)

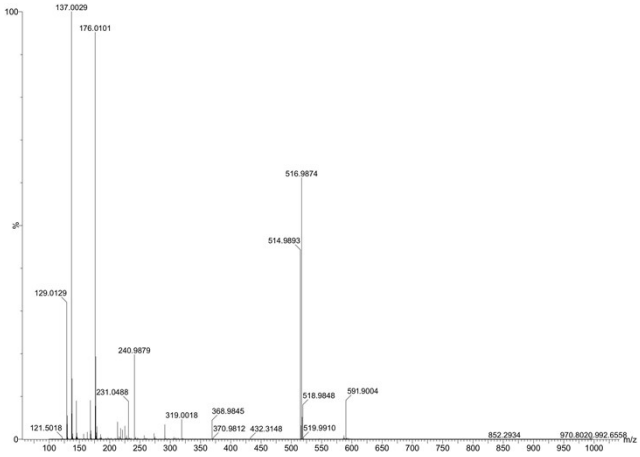

Figure S6. HRMS spectra of Ni(II) complex (**2**).

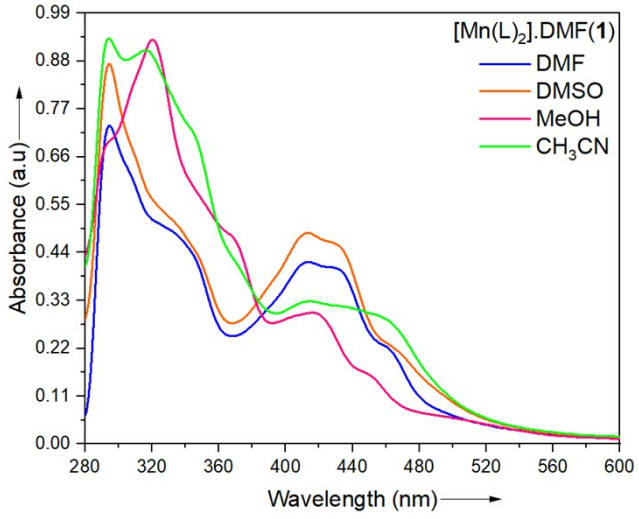

Figure S7. UV-Vis spectrum of Mn(III) complex (**1**) in different solvents at room temperature.

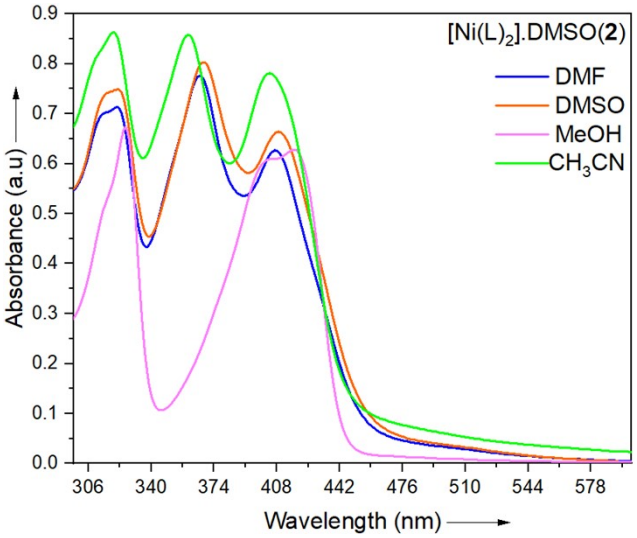

Figure S8. UV-Vis spectrum of Ni(II) complex (**2**) in different solvents at room temperature.

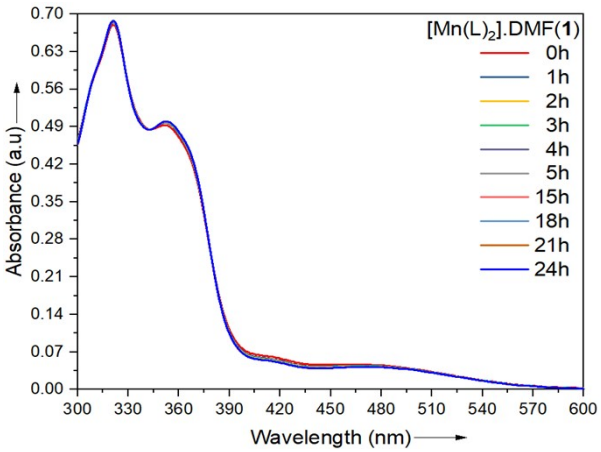

Figure S9. Time dependent absorption spectra of Mn(III) complex (**1**) in buffer solution (pH=7.4).

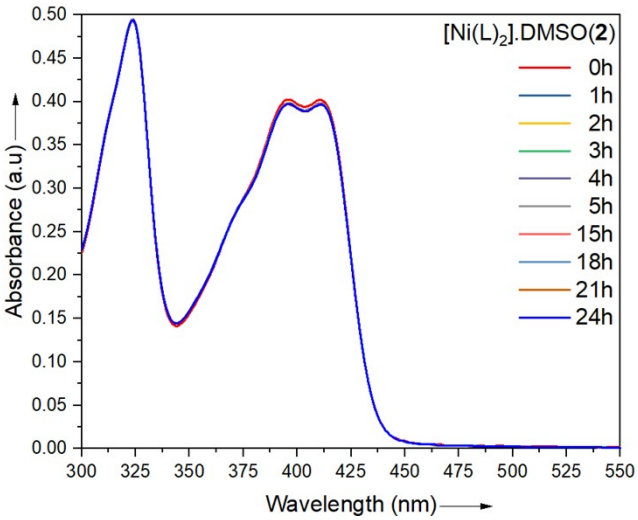

Figure S10. Time dependent absorption spectra of Ni(II) complex (**2**) in buffer solution (pH=7.4).

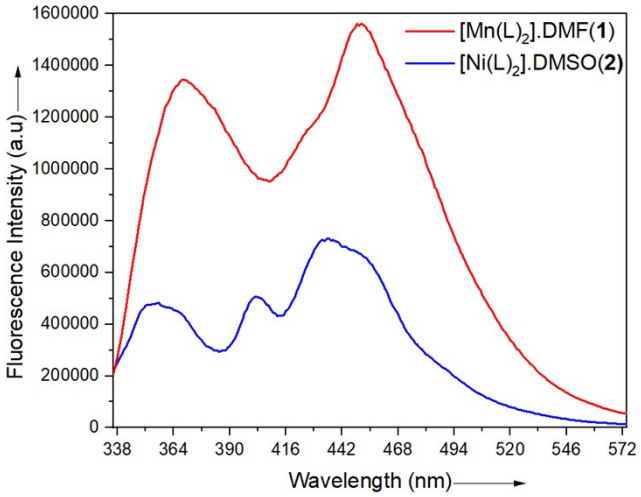

Figure S11. Fluorescence spectra of the Mn(III)complex (**1**) and the Ni(II) complex (**2**) at room temperature in MeOH.

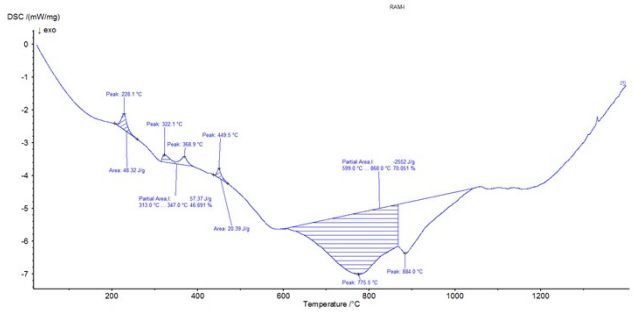

Figure S12. DSC thermal analysis of the Mn(III) complex (**1**).

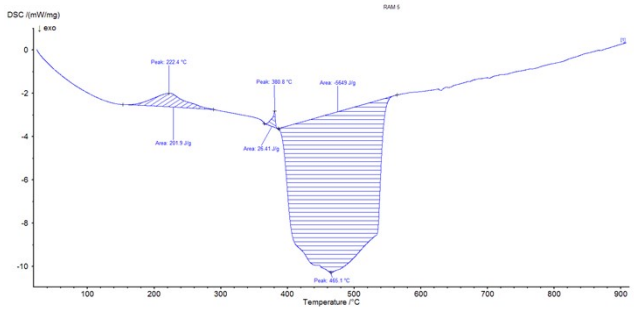

Figure S13. DSC thermal analysis of the Ni(II) complex (**2**).

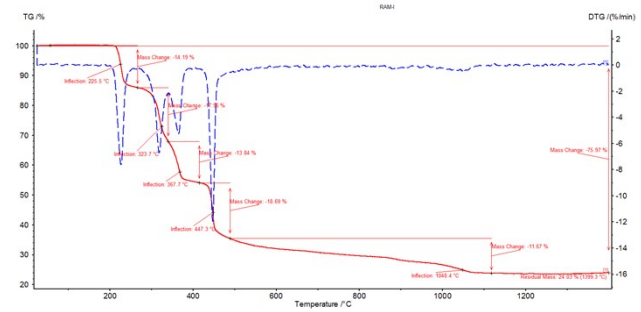

Figure S14. TG-DTG thermal analysis of the Mn(III)complex (**1**).

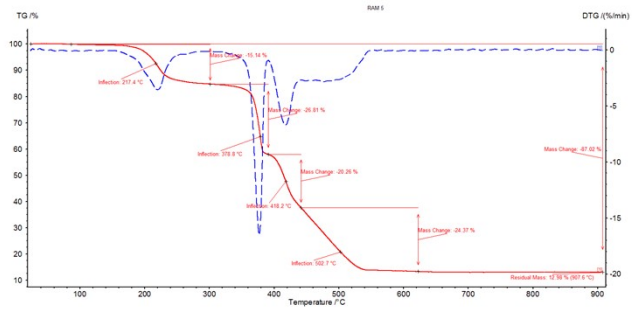

Figure S15. TG-DTG thermal analysis of the Ni(II) complex (**2**).

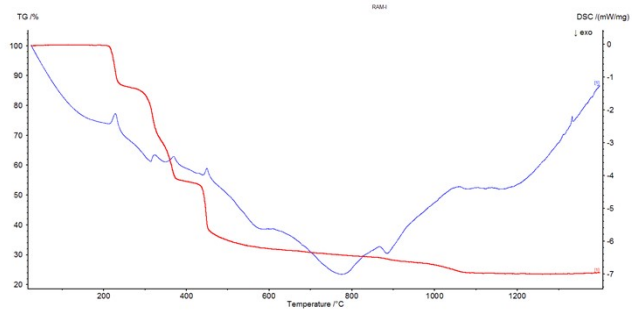

Figure S16. TG-DSC thermal analysis of the Mn(III) complex (**1**).

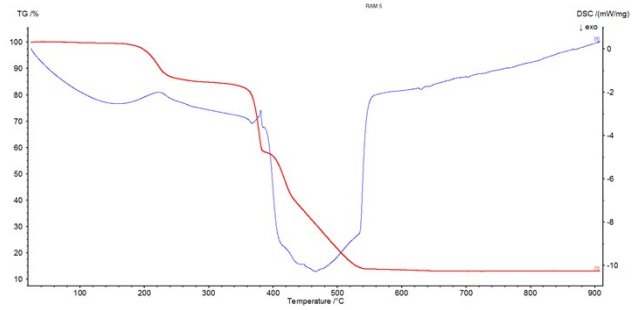

Figure S17. TG-DSC thermal analysis of the Ni(II) complex (**2**).

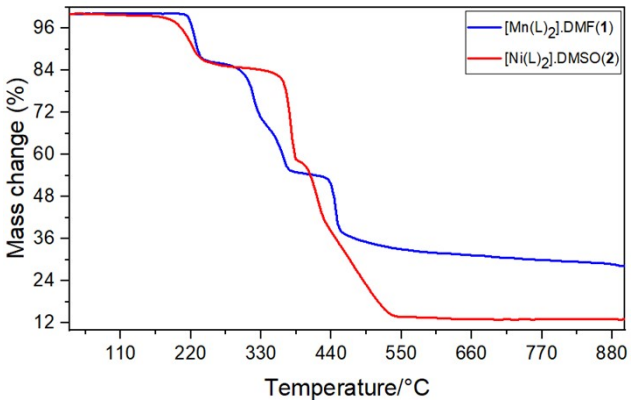

Figure S18. Mass loss comparison plots of the Mn(III) complex (**1**) and Ni(II) complex (**2**).

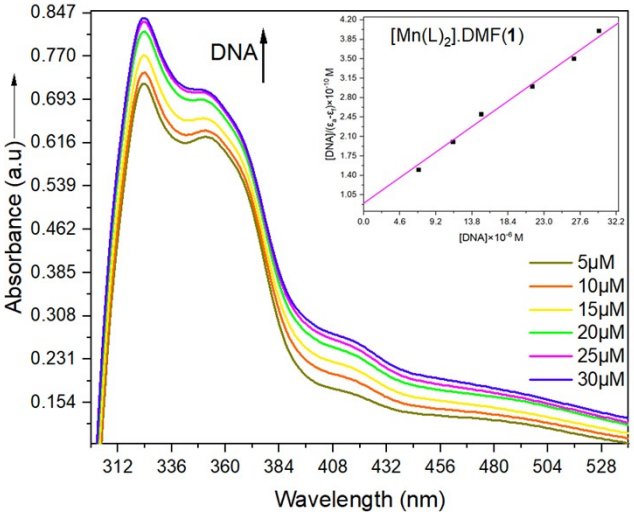

Figure S19. Absorption titration spectra upon incremental addition of CT-DNA to Mn(III) complex (**1**) solution [Inset: the linear fitting to determine binding constant].

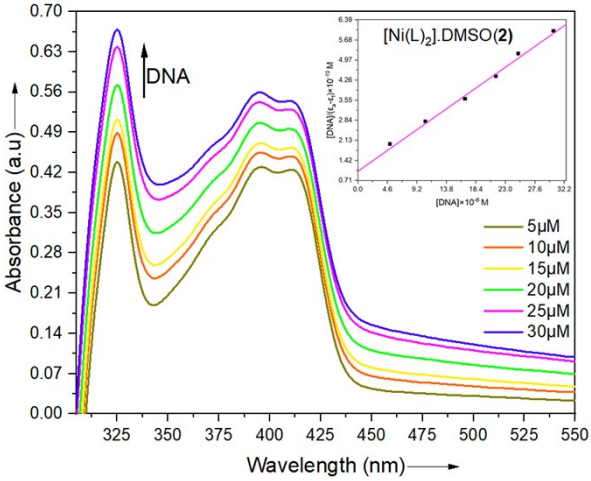

Figure S20. Absorption titration spectra upon incremental addition of CT-DNA to Ni(II) complex (**2**) solution [Inset: the linear fitting to determine binding constant].

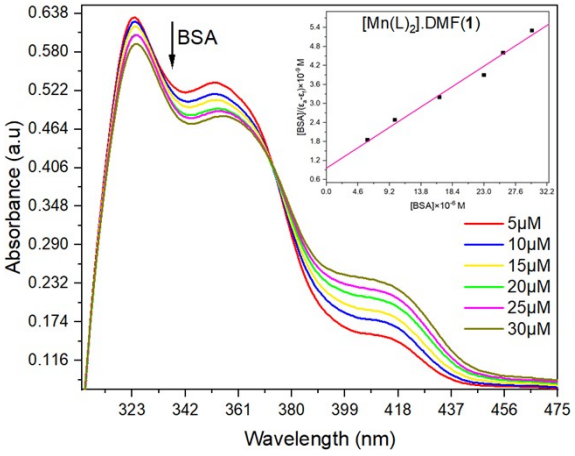

Figure S21. Absorption titration spectra upon incremental addition of BSA to Mn(III) complex (**1**) solution [Inset: the linear fitting to determine binding constant].

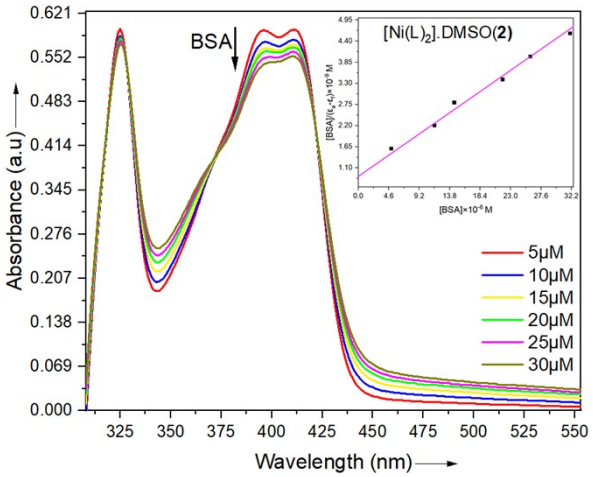

Figure S22. Absorption titration spectra upon incremental addition of BSA to Ni(II) complex (**2**) solution [Inset: the linear fitting to determine binding constant].

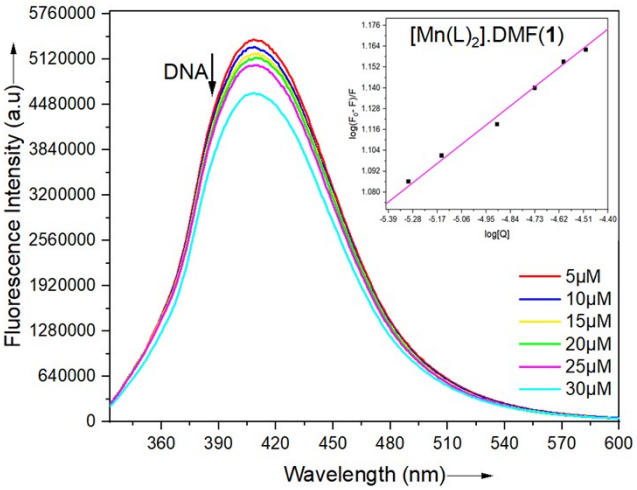

Figure S23. Fluorescence spectra of the Mn(III)complex (**1**) with DNA at room temperature.

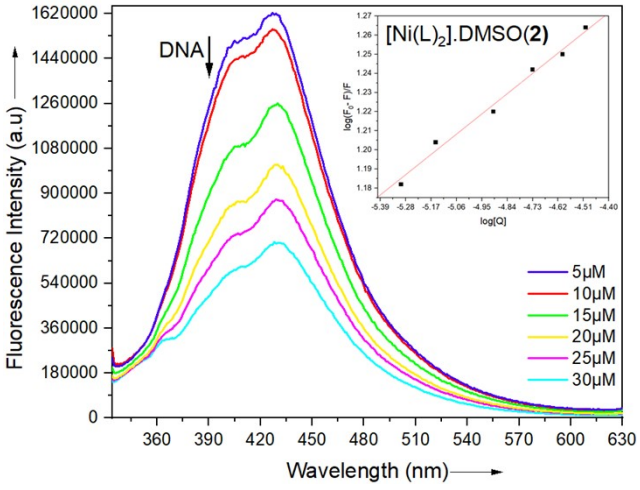

Figure S24. Fluorescence spectra of the Ni(II) complex (**2**) with DNA at room temperature.

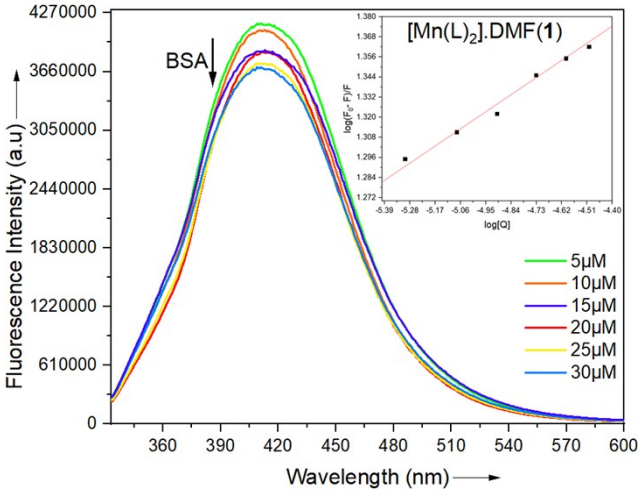

Figure S25. Fluorescence spectra of the Mn(III)complex (**1**) with BSA at room temperature.

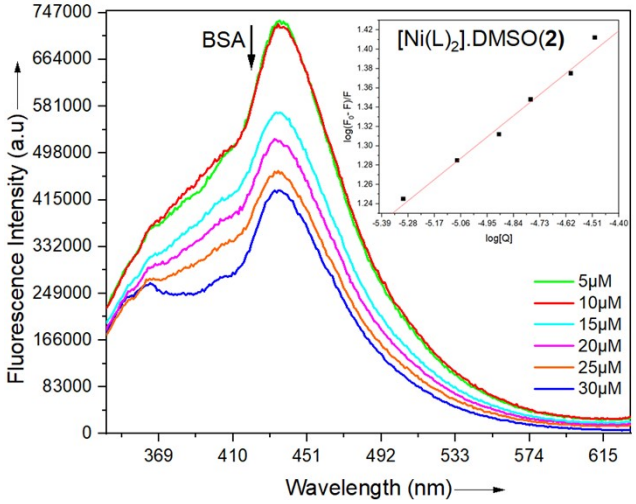

Figure S26. Fluorescence spectra of the Ni(II) complex (**2**) with BSA at room temperature.

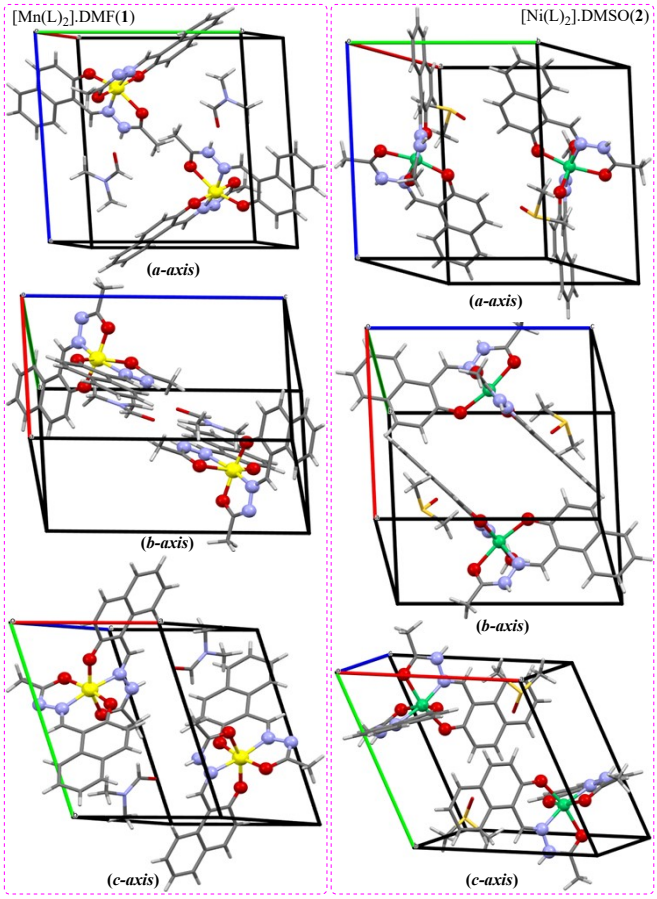

Figure S27. The packing view of Mn(III) complex (**1**) and Ni(II) complex (**2**) (along a-c axis).

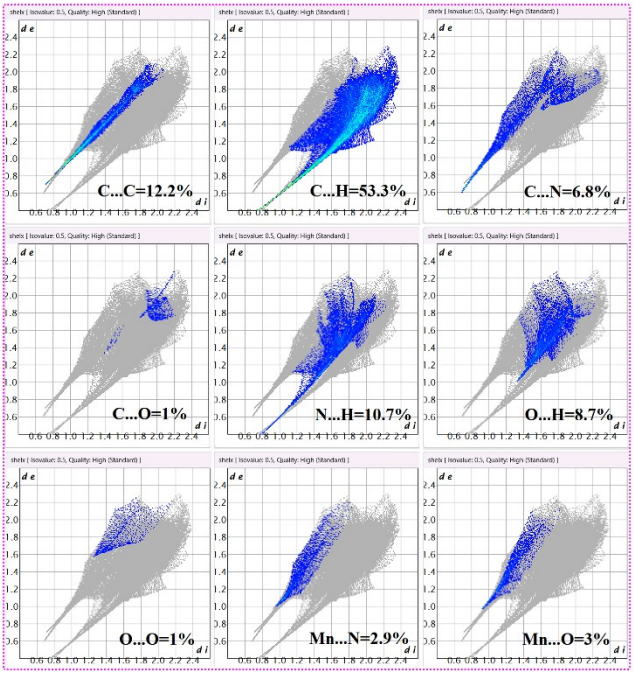

Figure S28. Fingerprint plot for Mn(III) complex (**1**) showing the percentage of contact that contributed to the total Hirshfeld surface (HS) area of the molecules and its pie chart; d_i, and d_e are

the distances from the surface to the nearest atoms interior and exterior to the surface, respectively.

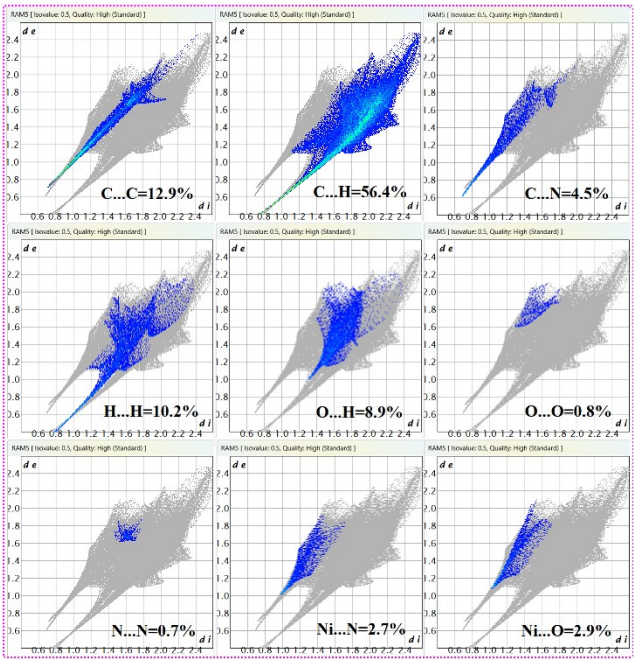

Figure S29. Fingerprint plot for Ni(II) complex (**2**) showing the percentage of contact that contributed to the total Hirshfeld surface (HS) area of the molecules and its pie chart; d_i, and d_e are the distances from the surface to the nearest atoms interior and exterior to the surface, respectively.

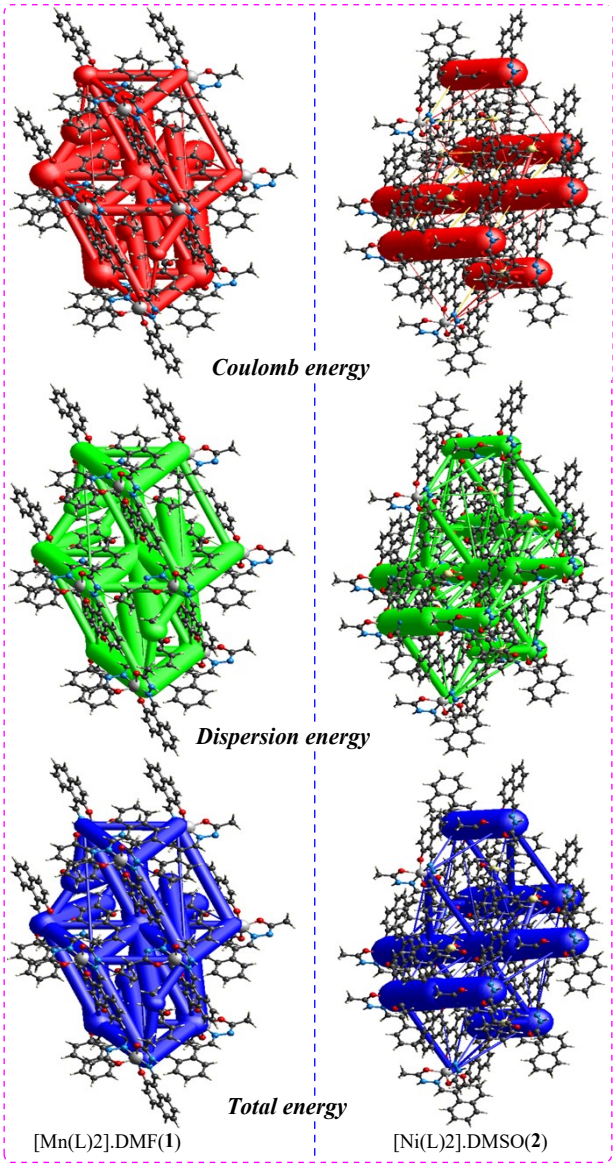

Figure S30. The 3D graphical representation of energy framework diagrams for the Mn(III) complex (**1**) and Ni(II) complex (**2**).

Interaction Energies (kJ/mol)
R is the distance between molecular centroids (mean atomic position) in Å.

Total energies, only reported for two benchmarked energy models, are the sum of the four energy components, scaled appropriately (see the scale factor table below)

	N	Symop	R	Electron Density	E_ele	E_pol	E_dis	E_rep	E_tot
	2	x, y, z	8.39	B3LYP/6-31G(d,p)	-12.7	-6.3	-35.0	36.0	-26.3
	2	x, y, z	12.45	B3LYP/6-31G(d,p)	-9.1	-2.5	-25.5	0.0	-33.6
	1	-x, -y, -z	10.35	B3LYP/6-31G(d,p)	-32.1	-12.4	-64.0	42.9	-72.3
	1	-	8.14	B3LYP/6-31G(d,p)	0.0	nan	0.0	0.0	nan
	1	-	7.24	B3LYP/6-31G(d,p)	-1.9	-0.5	-2.2	0.0	-4.2
	2	x, y, z	11.98	B3LYP/6-31G(d,p)	0.0	0.0	0.0	0.0	0.0
	1	-x, -y, -z	16.53	B3LYP/6-31G(d,p)	-1.4	-0.3	-7.4	0.0	-8.1
	1	-x, -y, -z	8.36	B3LYP/6-31G(d,p)	-16.5	-4.6	-72.3	52.6	-51.3
	1	-x, -y, -z	9.94	B3LYP/6-31G(d,p)	3.9	-3.4	-13.2	3.1	-7.9
	1	-x, -y, -z	8.58	B3LYP/6-31G(d,p)	-7.2	-6.4	-69.9	44.1	-46.0
	1	-x, -y, -z	9.38	B3LYP/6-31G(d,p)	-23.5	-5.0	-31.9	21.3	-43.1
	1	-	6.50	B3LYP/6-31G(d,p)	-3.4	-2.5	-25.5	0.0	-27.6
	1	-	5.93	B3LYP/6-31G(d,p)	-12.7	-6.3	-35.0	36.0	-26.3
	1	-x, -y, -z	9.91	B3LYP/6-31G(d,p)	-3.3	-0.7	-10.4	3.1	-11.2
	1	-	12.11	B3LYP/6-31G(d,p)	-16.5	-4.6	-72.3	52.6	-51.3
	1	-	7.84	B3LYP/6-31G(d,p)	-32.1	-12.4	-64.0	42.9	-72.3

Scale factors for benchmarked energy models
See Mackenzie et al. IUCrJ (2017)

$[Mn(L)_2]\cdot DMF(\mathbf{1})$

Energy Model	k_ele	k_pol	k_disp	k_rep
CE-HF ... HF/3-21G electron densities	1.019	0.651	0.901	0.811
CE-B3LYP ... B3LYP/6-31G(d,p) electron densities	1.057	0.740	0.871	0.618

Interaction Energies (kJ/mol)
R is the distance between molecular centroids (mean atomic position) in Å.

Total energies, only reported for two benchmarked energy models, are the sum of the four energy components, scaled appropriately (see the scale factor table below)

	N	Symop	R	Electron Density	E_ele	E_pol	E_dis	E_rep	E_tot
	0	-	6.22	B3LYP/6-31G(d,p)	-22.1	-5.8	-25.0	27.4	-32.5
	0	-	5.62	B3LYP/6-31G(d,p)	-26.8	-8.4	-35.3	33.9	-44.5
	0	x, y, z	12.48	B3LYP/6-31G(d,p)	-3.3	-2.9	-36.3	0.0	-37.3
	0	-x, -y, -z	13.64	B3LYP/6-31G(d,p)	-3.0	-3.6	-36.9	0.0	-38.0
	0	x, y, z	16.76	B3LYP/6-31G(d,p)	-0.4	-0.3	-9.8	0.0	-9.2
	0	-x, -y, -z	6.17	B3LYP/6-31G(d,p)	-191.8	-60.9	-107.8	235.2	-196.5
	0	x, y, z	10.63	B3LYP/6-31G(d,p)	-5.7	-1.2	-12.0	4.4	-14.6
	0	-x, -y, -z	9.56	B3LYP/6-31G(d,p)	7.3	-1.5	-16.8	6.4	-4.1
	0	x, y, z	11.55	B3LYP/6-31G(d,p)	6.1	-0.7	-2.5	0.1	3.8
	0	-	10.36	B3LYP/6-31G(d,p)	-5.9	-1.1	-10.5	13.4	-7.9
	0	-x, -y, -z	5.43	B3LYP/6-31G(d,p)	-197.6	-62.1	-141.5	266.0	-213.8
	0	x, y, z	10.96	B3LYP/6-31G(d,p)	-2.9	-0.8	-5.6	1.6	-7.6
	0	-	8.74	B3LYP/6-31G(d,p)	-8.0	-1.5	-13.4	10.0	-15.1
	0	-	6.69	B3LYP/6-31G(d,p)	5.6	-1.2	-6.7	2.2	0.6
	0	-	11.22	B3LYP/6-31G(d,p)	-3.0	-1.0	-12.4	14.2	-6.0
	0	-x, -y, -z	8.71	B3LYP/6-31G(d,p)	5.5	-2.2	-19.3	4.5	-9.8
	0	-x, -y, -z	15.85	B3LYP/6-31G(d,p)	0.3	-0.2	-8.0	0.0	-6.9
	0	-	7.83	B3LYP/6-31G(d,p)	-0.6	-4.9	-7.1	10.9	-3.8

Scale factors for benchmarked energy models
See Mackenzie et al. IUCrJ (2017)

$[Ni(L)_2]\cdot DMSO(\mathbf{2})$

Energy Model	k_ele	k_pol	k_disp	k_rep
CE-HF ... HF/3-21G electron densities	1.019	0.651	0.901	0.811
CE-B3LYP ... B3LYP/6-31G(d,p) electron densities	1.057	0.740	0.871	0.618

Figure S31. Energy framework CE-B3LYP estimates of energy components and total energies (kJ/mol) for the closest intermolecular interactions in the Mn(III) complex (**1**) and Ni(II) complex (**2**).

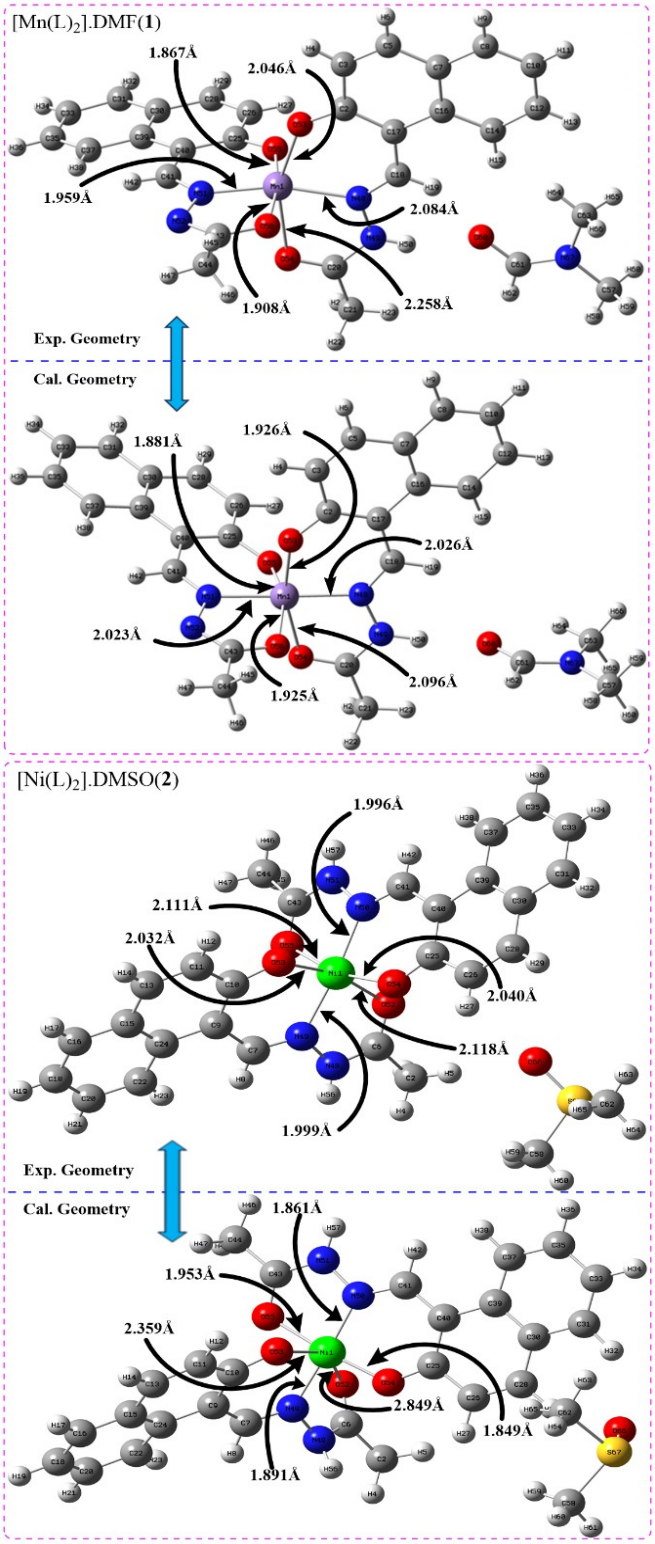

Figure S32. The calculated (Cal.) optimized geometry and experimental (Exp.) single crystal geometry for Mn(III) complex (**1**) and Ni(II) complex (**2**).

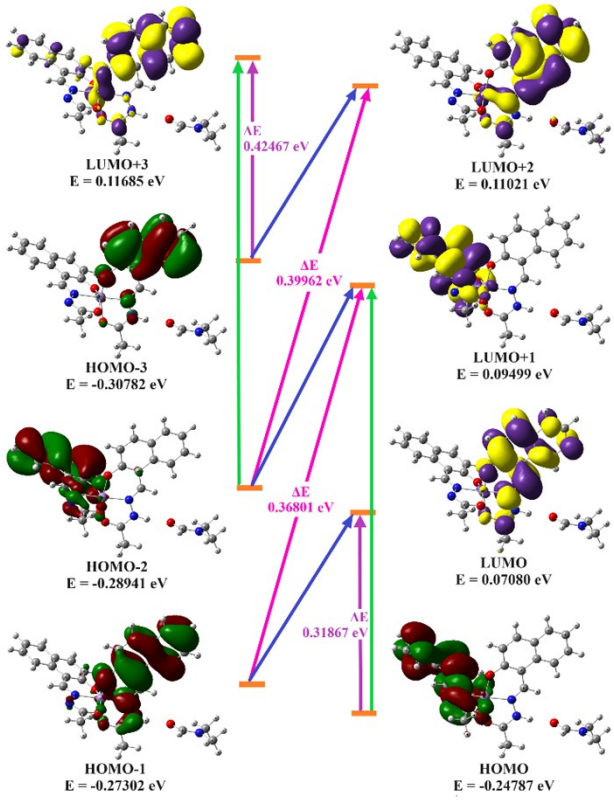

Figure S33. DFT calculated HOMO-LUMO molecular orbital energy level diagram of the Mn(III) complex (**1**).

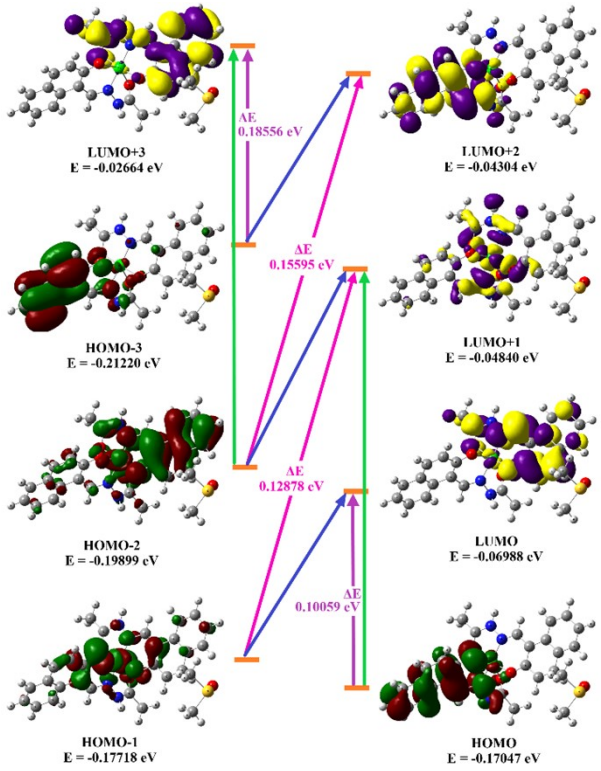

Figure S34. DFT calculated HOMO-LUMO molecular orbital energy level diagram of the Ni(II) complex (**2**).

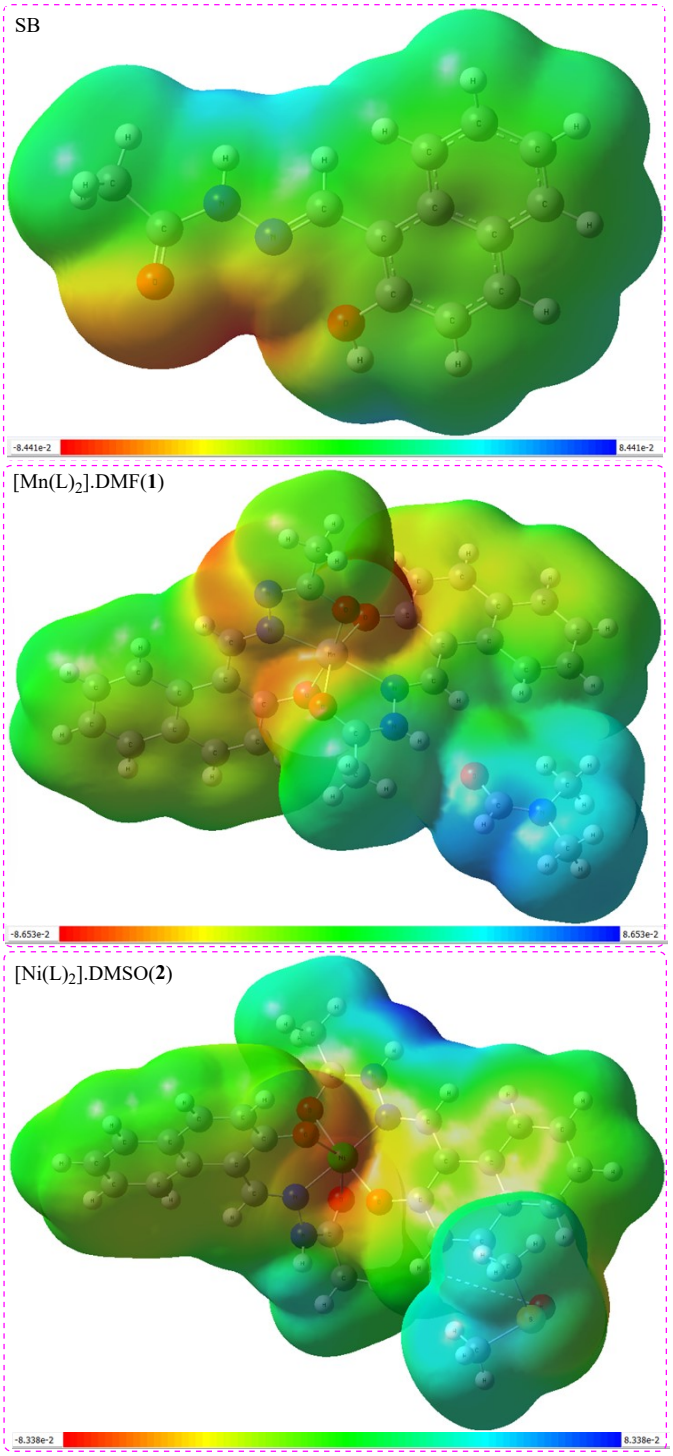

Figure S35. The molecular electrostatic potential (MEPs) surfaces of the Schiff base (SB) ligand and its Mn(III) complex (**1**) and Ni(II) complex (**2**).

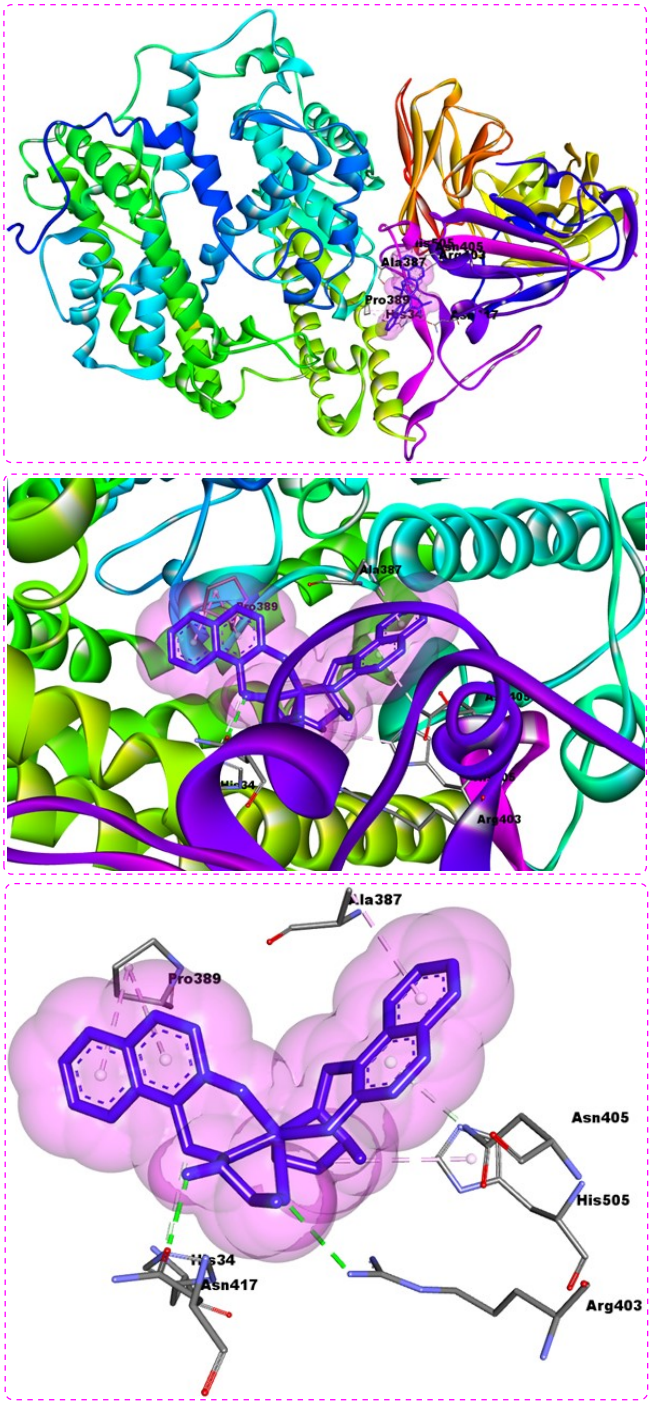

Figure S36. Docked view of Ni(II) complex (**2**) inside the active site of the SARS-CoV-2 spike-RBD protein(PDB ID: 8FXC) with its focussed view for interacting amino acid residues.

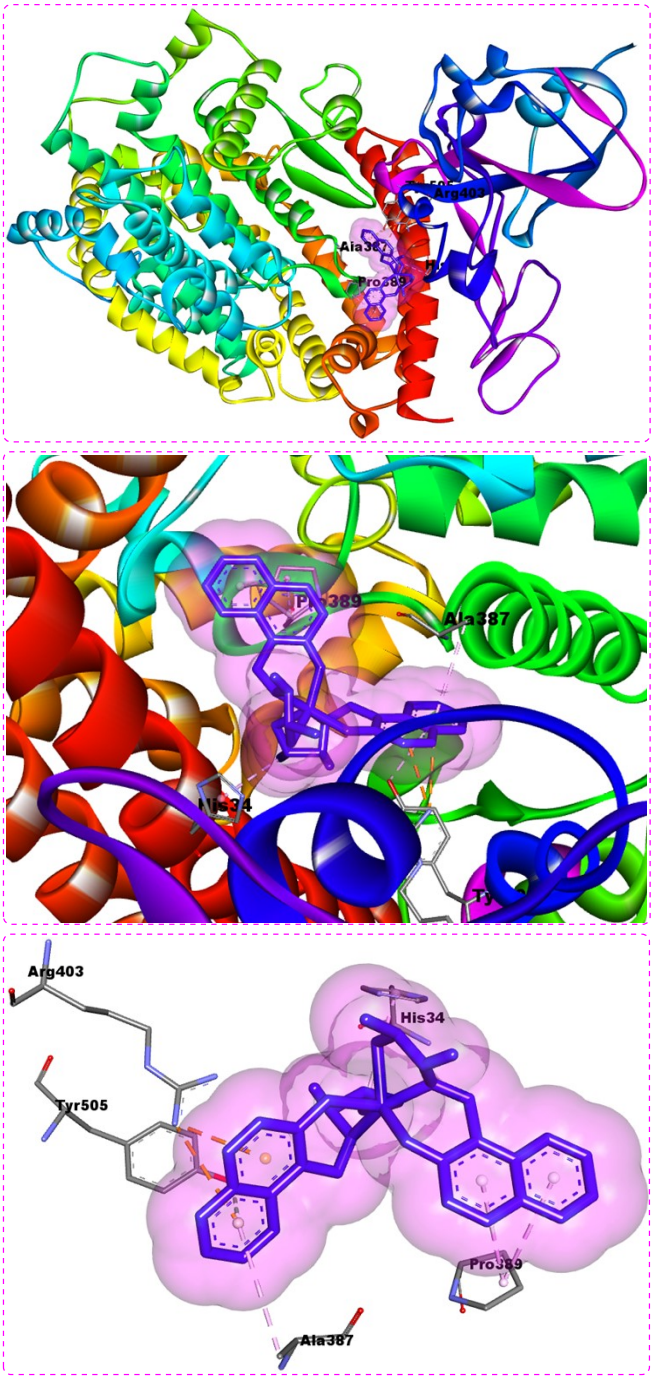

Figure S37. Docked view of Ni(II) complex (**2**) inside the active site of the SARS-CoV-2 spike-RBD protein(PDB ID: 6M0J) with its focussed view for interacting amino acid residues.

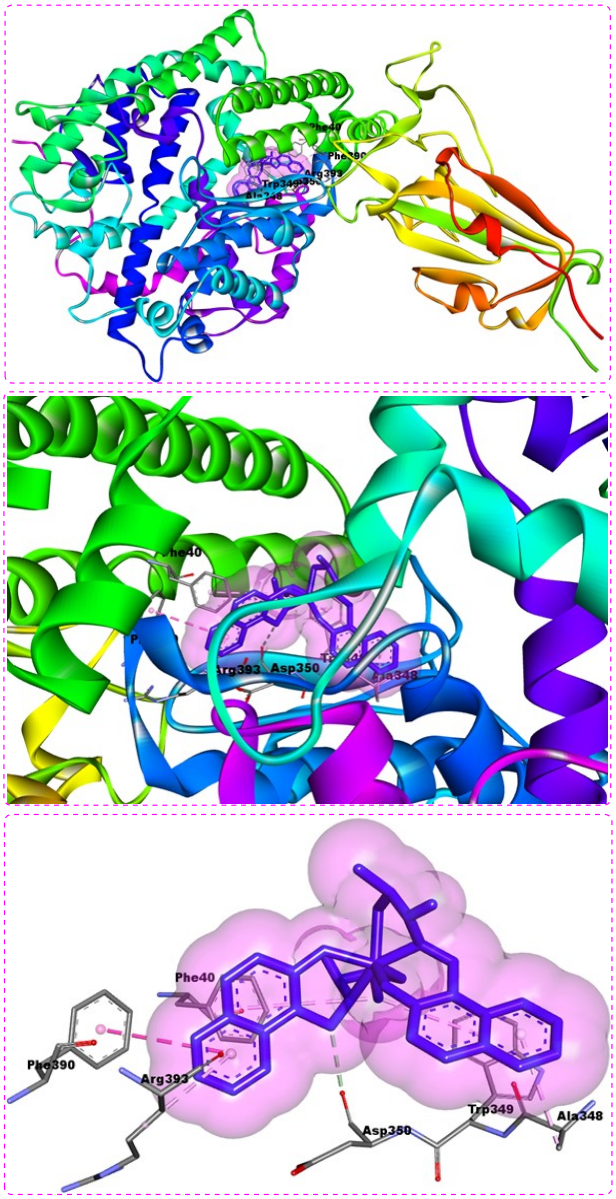

Figure S38. Docked view of Ni(II) complex (**2**) inside the active site of the SARS-CoV-2 spike-RBD protein (PDB ID: 8DV1) with its focussed view for interacting amino acid residues.

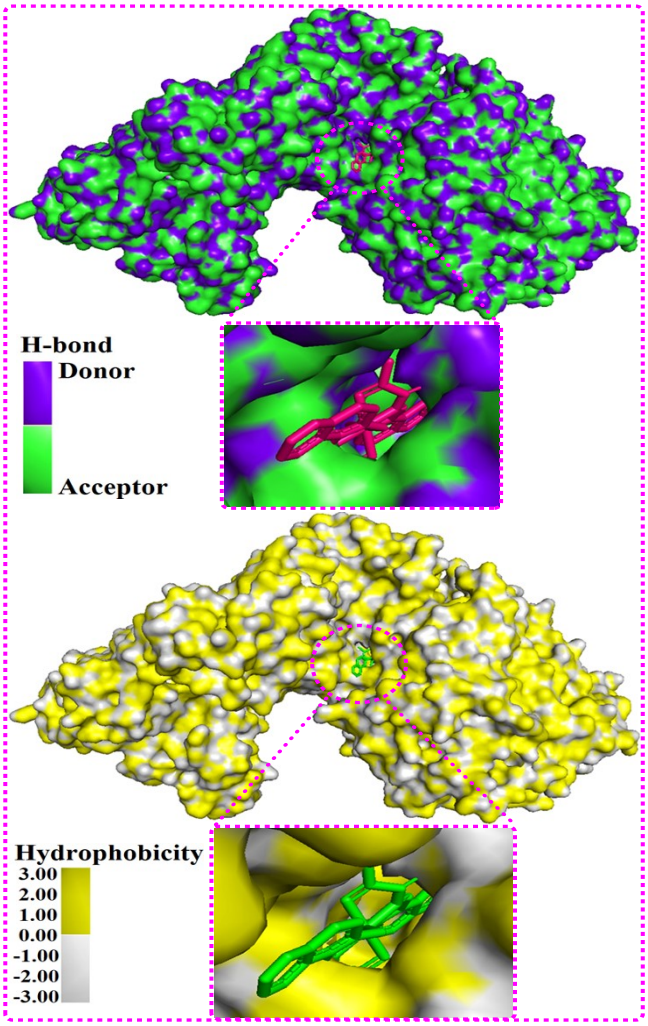

Figure S39. Docked view of total density surfaces with H-bond (top figure) and Hydrophobicity (bottom figure) of the docked Mn(III) complex (**1**) inside the active site of the SARS-CoV-2 spike-RBD protein (PDB ID: 8FXC).

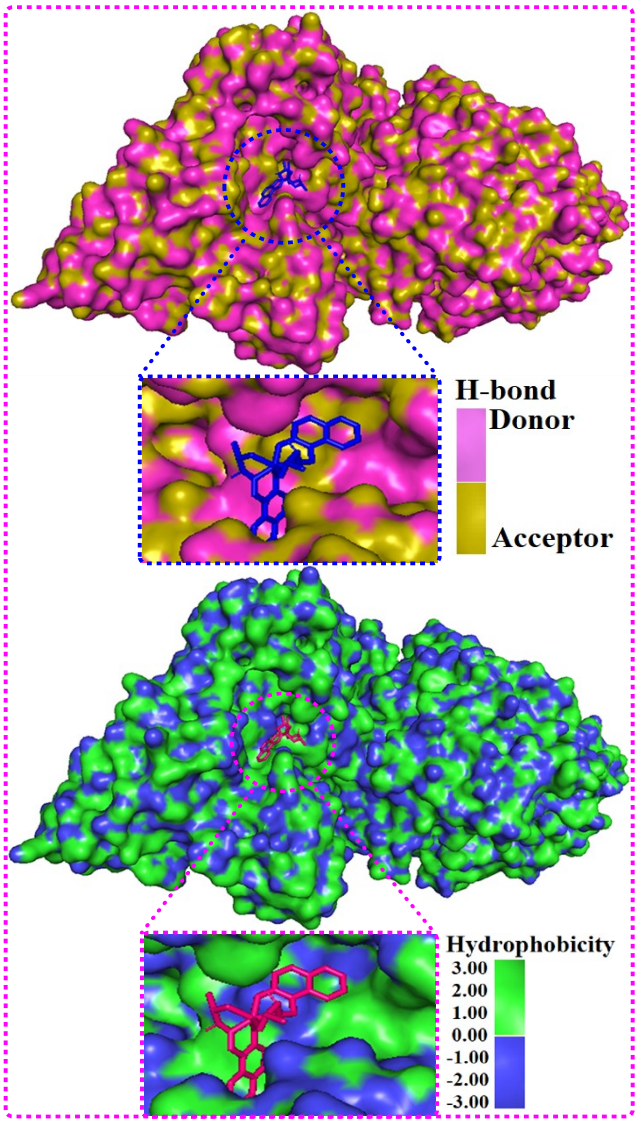

Figure S40. Docked view of total density surfaces with H-bond (top figure) and Hydrophobicity (bottom figure) of the docked Ni(II) complex (**2**) inside the active site of the SARS-CoV-2 spike-RBD protein (PDB ID: 8FXC).

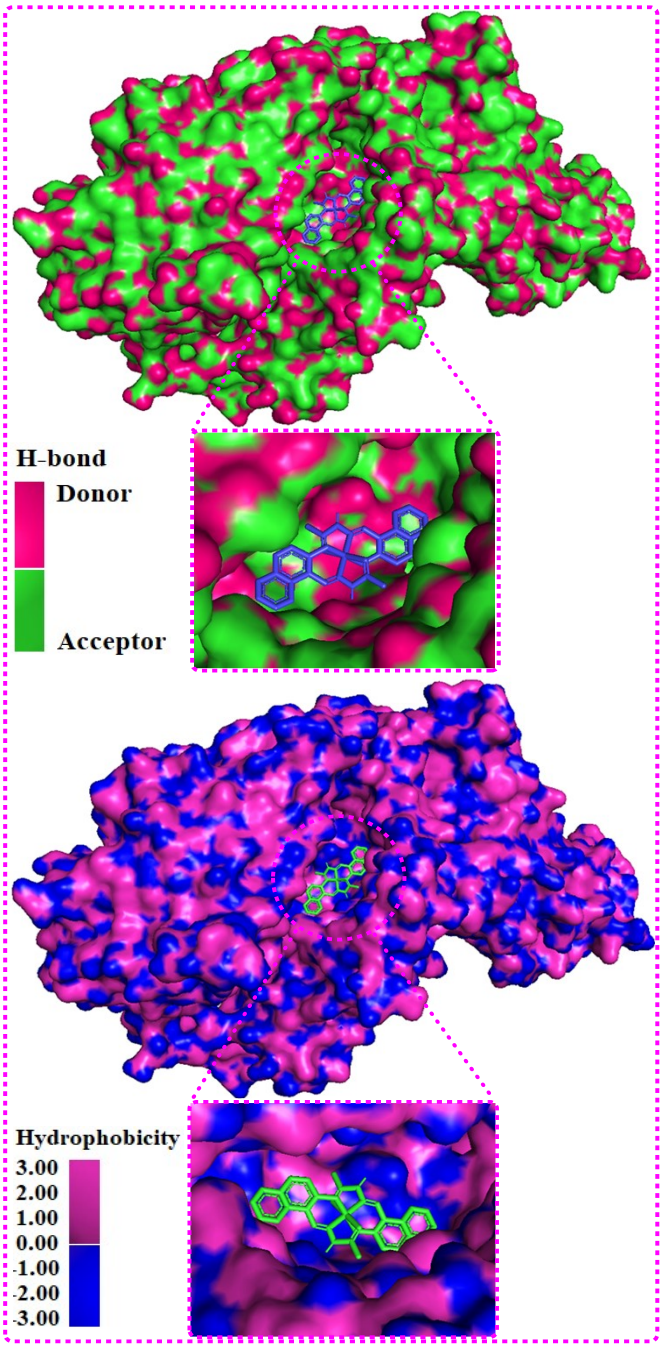

Figure 41. Docked view of total density surfaces with H-bond (top figure) and Hydrophobicity (bottom figure) of the docked Mn(III) complex (**1**) inside the active site of the SARS-CoV-2 spike-RBD protein(PDB ID: 6M0J).

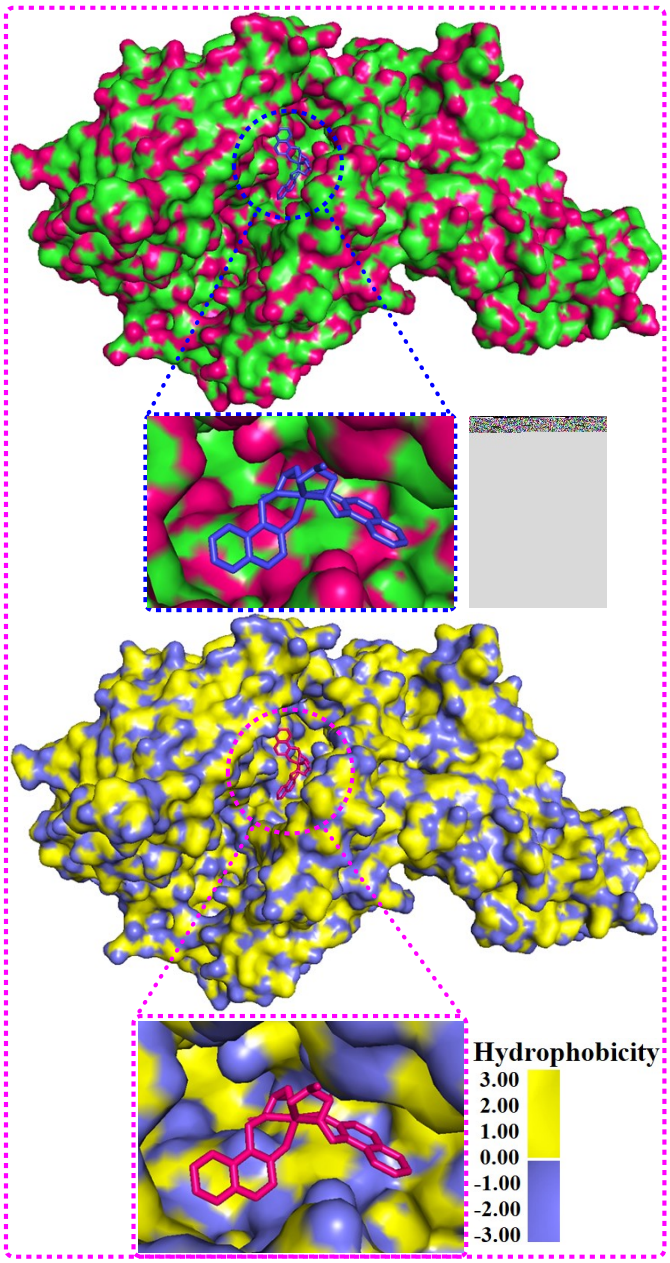

Figure S42. Docked view of total density surfaces with H-bond (top figure) and Hydrophobicity (bottom figure) of the docked Ni(II) complex (**2**) inside the active site of the SARS-CoV-2 spike-RBD protein(PDB ID: 6M0J).

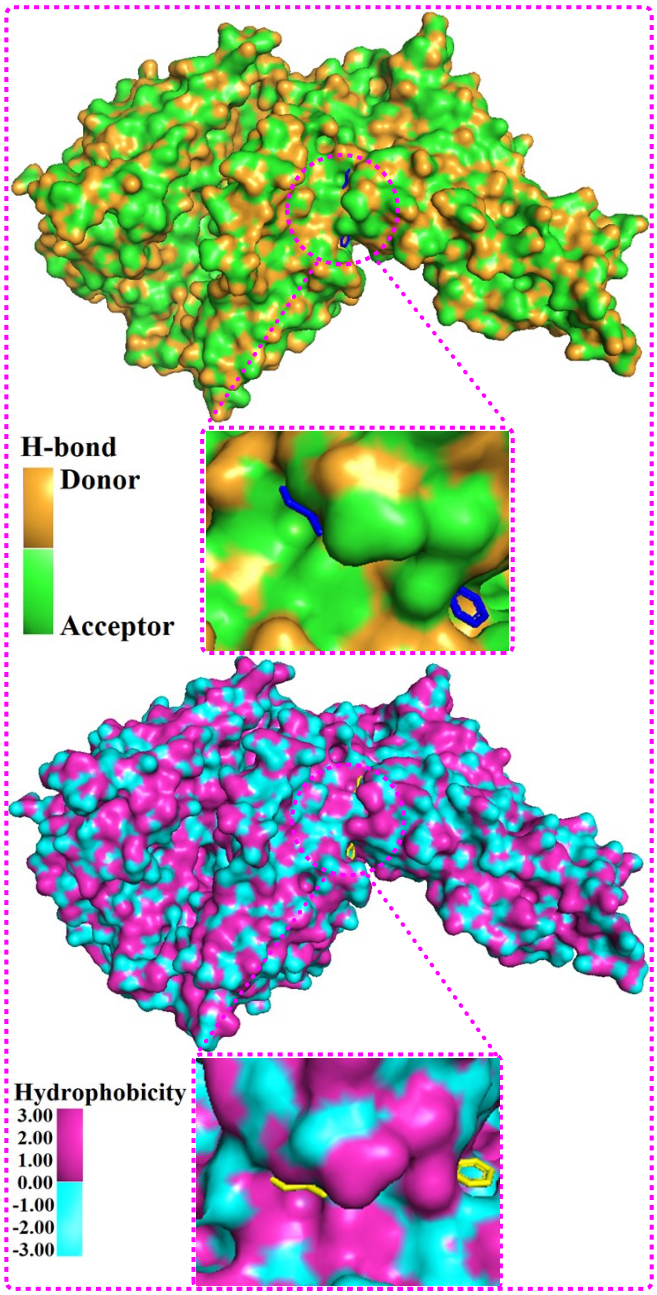

Figure S43. Docked view of total density surfaces with H-bond (top figure) and Hydrophobicity (bottom figure) of the docked Mn(III) complex (**1**) inside the active site of the SARS-CoV-2 spike-RBD protein(PDB ID: 8DV1).

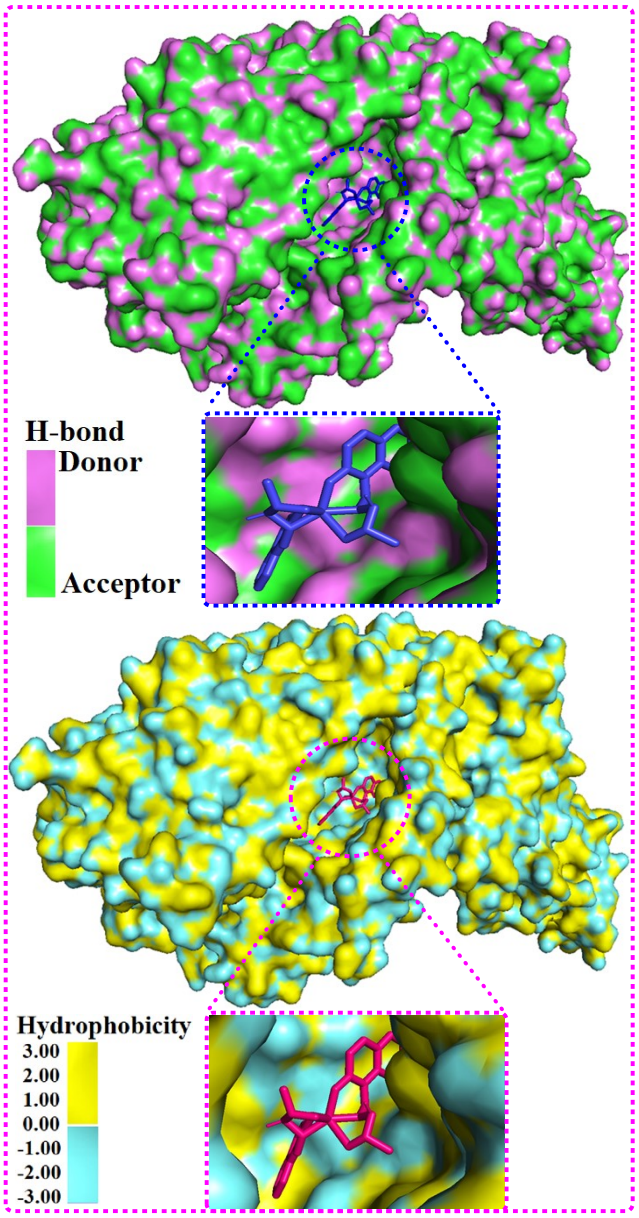

Figure S44. Docked view of total density surfaces with H-bond (top figure) and Hydrophobicity (bottom figure) of the docked Ni(II) complex (**2**) inside the active site of the SARS-CoV-2 spike-RBD protein(PDB ID: 8DV1).

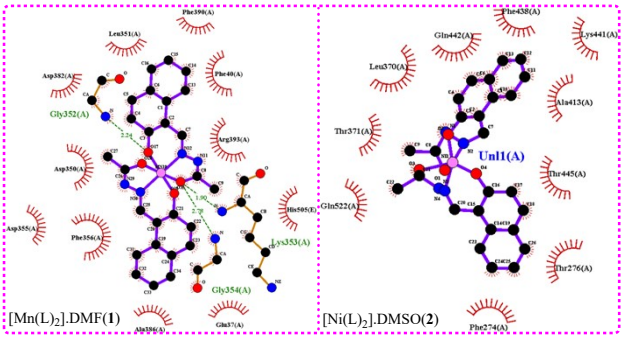

Figure S45. 3D view of the docked Mn(III) complex (**1**) and Ni(II) complex (**2**) with interacting residues inside the active site of the SARS-CoV-2 spike RBD protein (PDB ID: 8FXC).

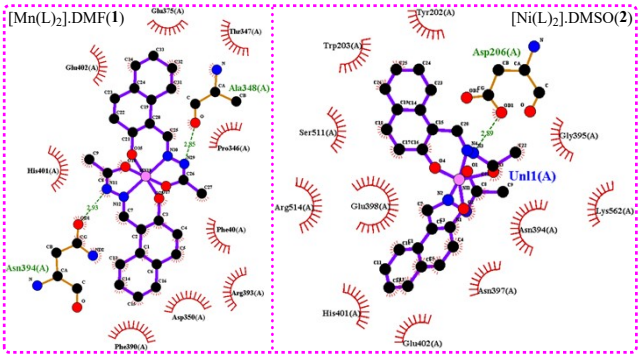

Figure S46. 3D view of the docked Mn(III) complex (**1**) and Ni(II) complex (**2**) with interacting residues inside the active site of the SARS-CoV-2 spike RBD protein (PDB ID: 6M0J).

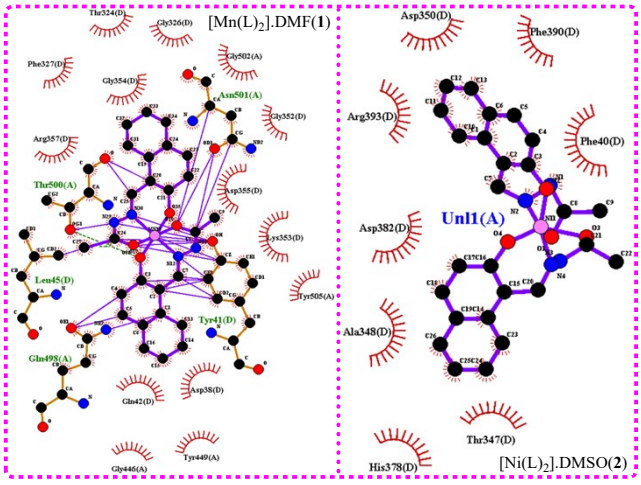

Figure S47. 3D view of the docked Mn(III) complex (**1**) and Ni(II) complex (**2**) with interacting residues inside the active site of the SARS-CoV-2 spike RBD protein (PDB ID: 8DV1).

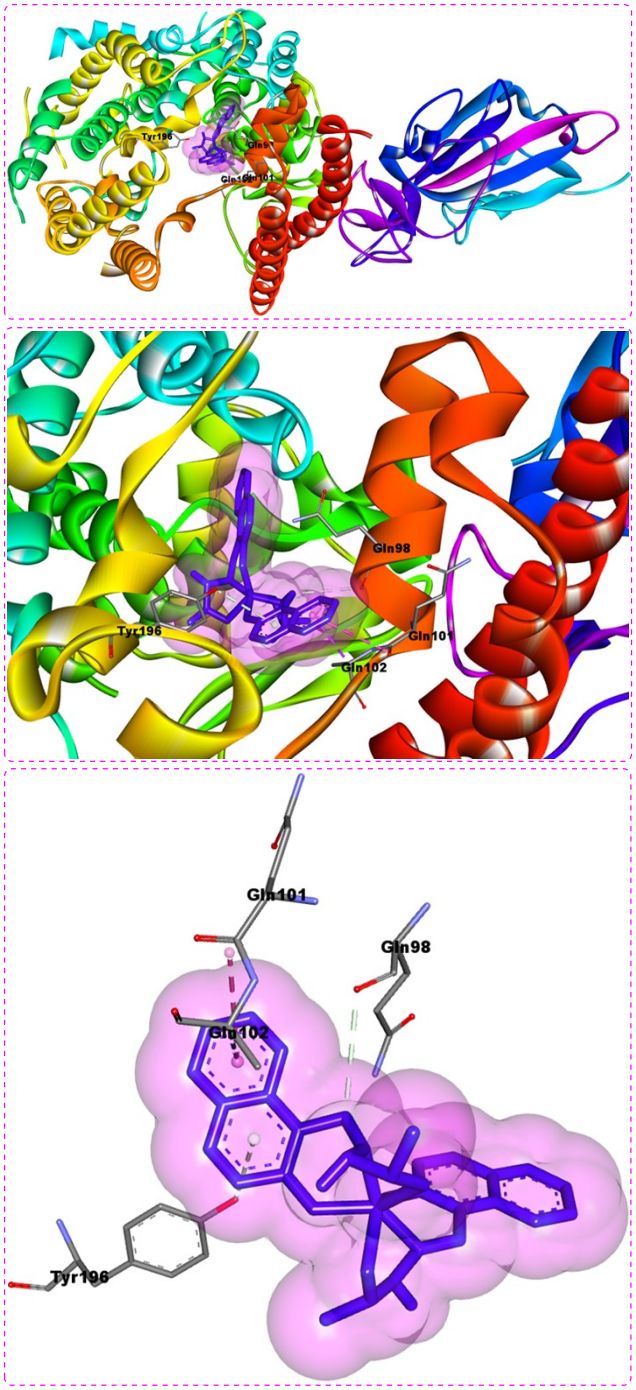

Figure S48. Docked view of Ni(II) complex (**2**) inside the active site of the SARS-CoV-2 Omicron RBD protein (PDB ID: 7TN0) with its focussed view for interacting amino acid residues.

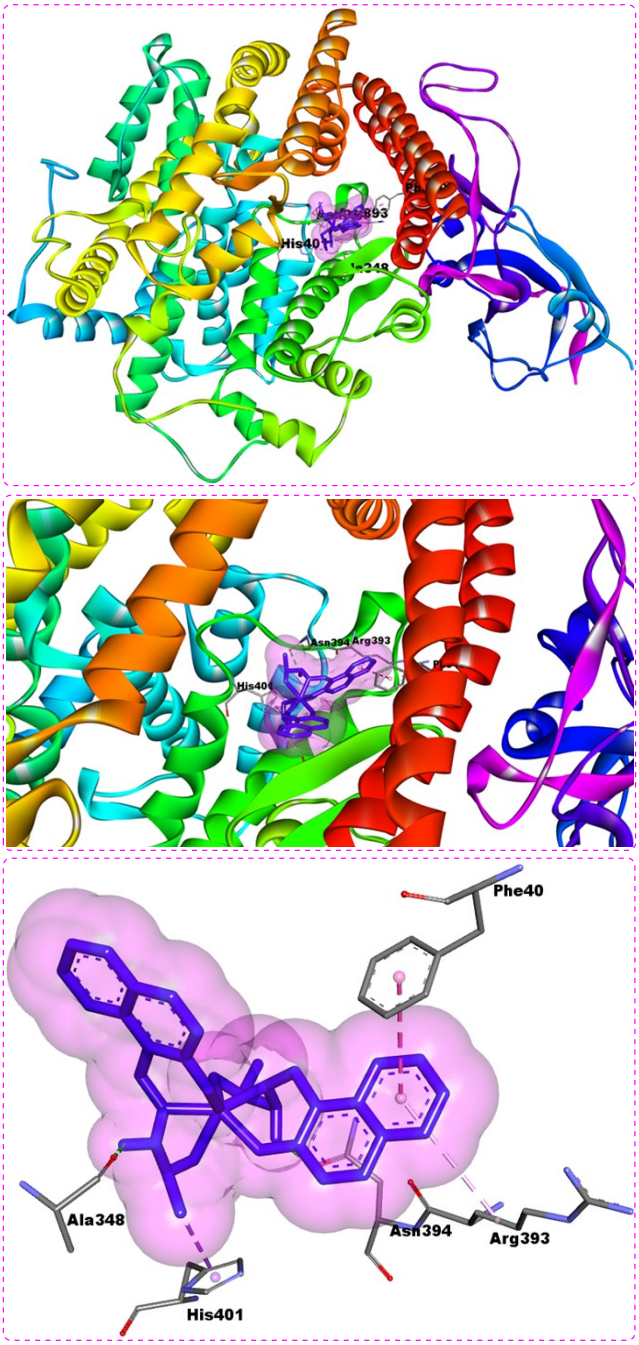

Figure S49. Docked view of Ni(II) complex (**2**) inside the active site of the SARS-CoV-2 Omicron variant spike glycoprotein (PDB ID: 7WBP) with its focussed view for interacting amino acid residues.

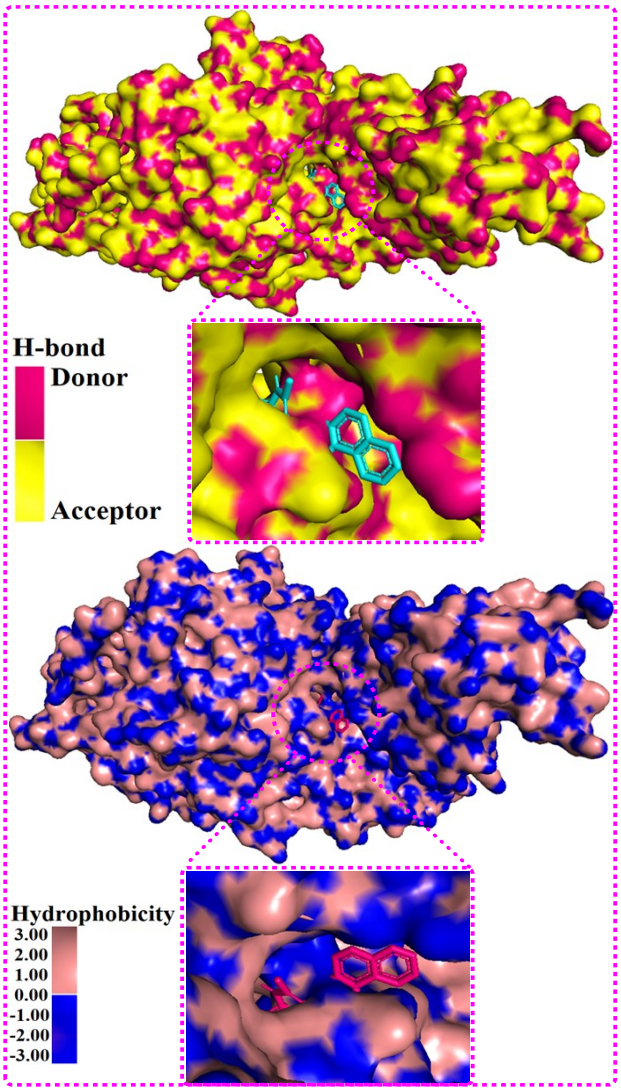

Figure S50. Docked view of total density surfaces with H-bond (top figure) and Hydrophobicity (bottom figure) of the docked Mn(III) complex (**1**) inside the active site of the SARS-CoV-2 Omicron RBD protein (PDB ID: 7TN0).

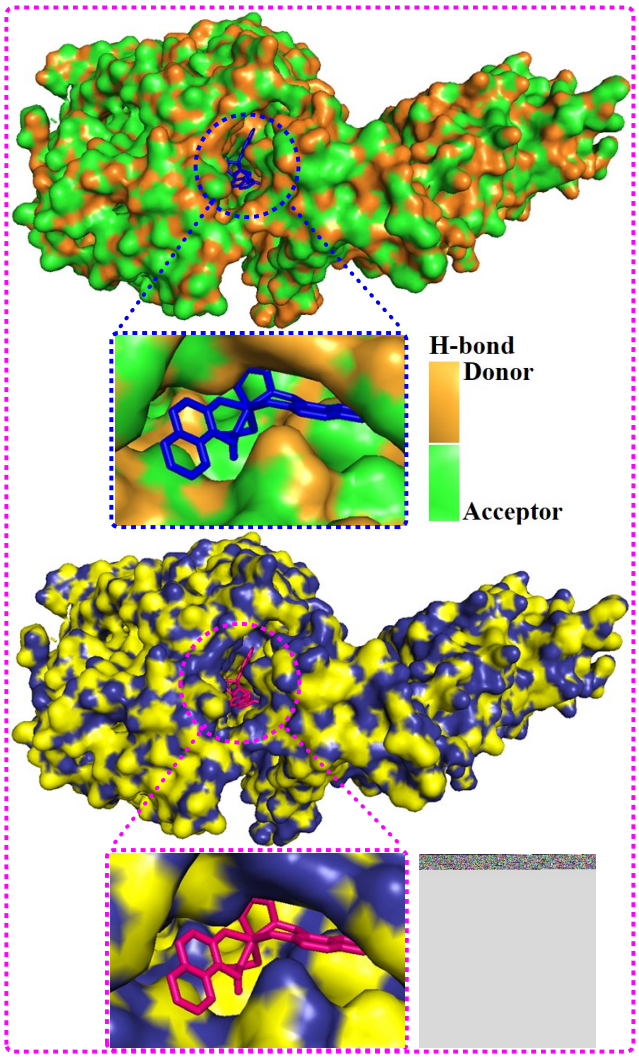

Figure S51. Docked view of total density surfaces with H-bond (top figure) and Hydrophobicity (bottom figure) of the docked Ni(II) complex (**2**) inside the active site of the SARS-CoV-2 Omicron RBD protein (PDB ID: 7TN0).

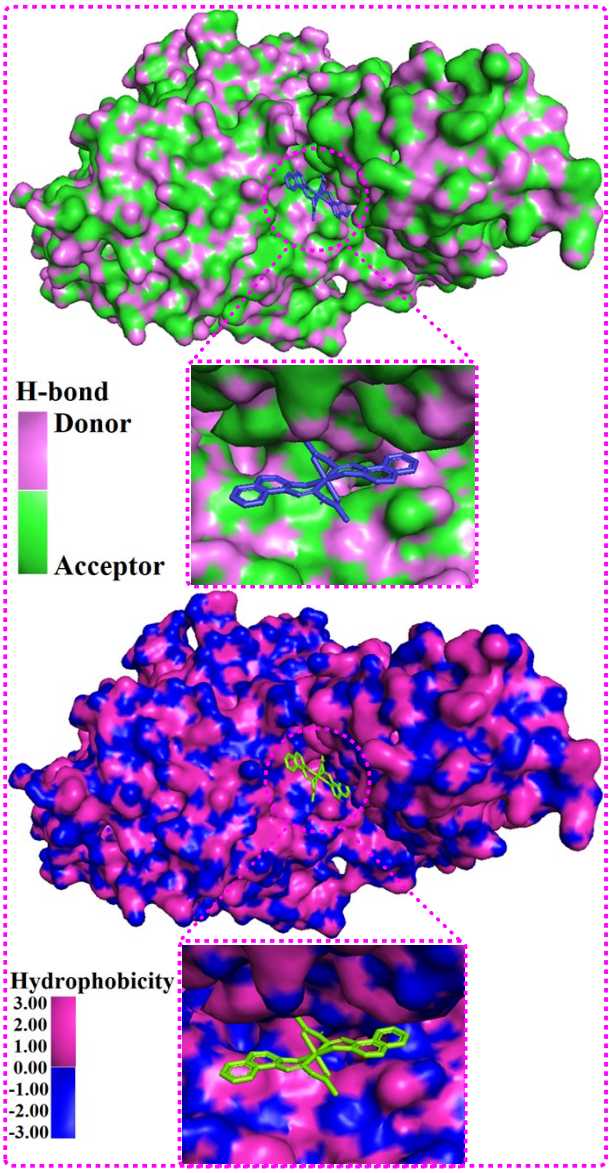

Figure S52. Docked view of total density surfaces with H-bond (top figure) and Hydrophobicity (bottom figure) of the docked Mn(III) complex (**1**) inside the active site of the SARS-CoV-2 Omicron RBD protein (PDB ID: 7WBP).

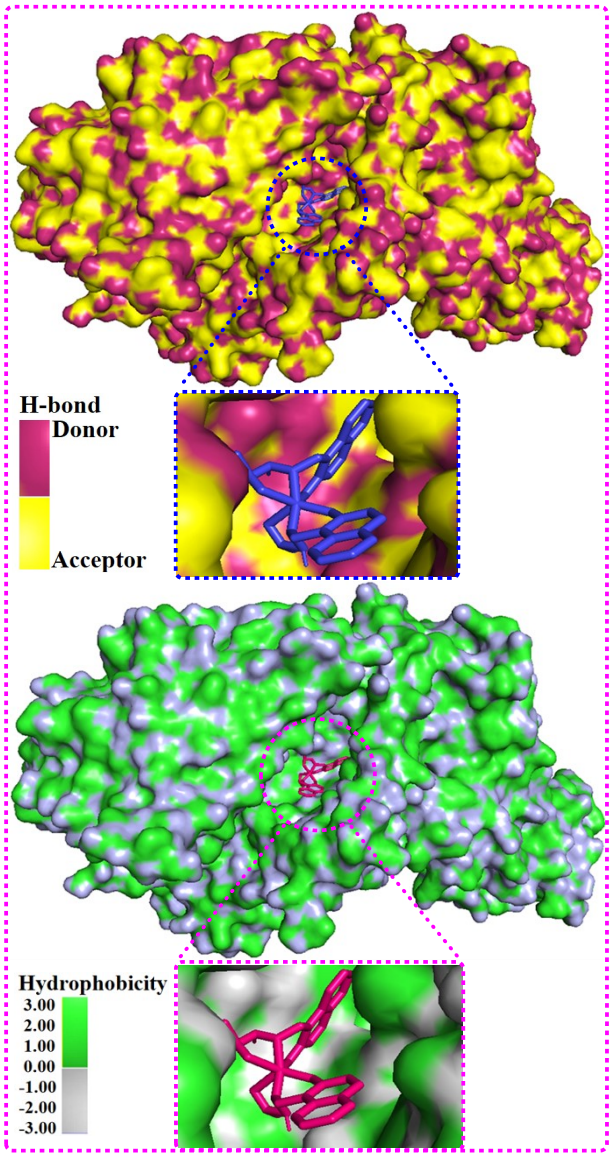

Figure S53. Docked view of total density surfaces with H-bond (top figure) and Hydrophobicity (bottom figure) of the docked Ni(II) complex (**2**) inside the active site of the SARS-CoV-2 Omicron RBD protein (PDB ID: 7WBP).

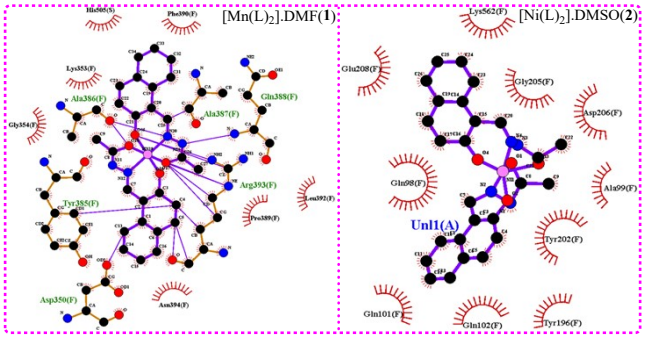

Figure S54. 3D view of the docked Mn(III) complex (**1**) and Ni(II) complex (**2**) with interacting residues inside the active site of the SARS-CoV-2 Omicron RBD protein (PDB ID: 7TN0).

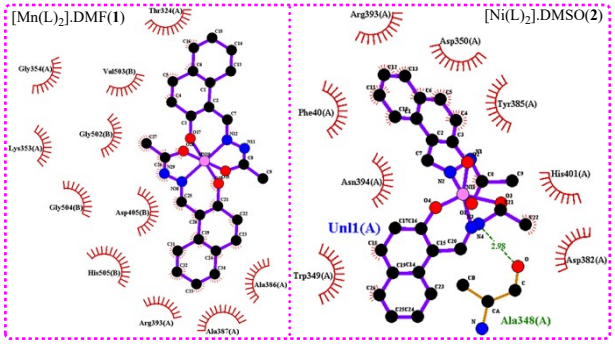

Figure S55. 3D view of the docked Mn(III) complex (**1**) and Ni(II) complex (**2**) with interacting residues inside the active site of the SARS-CoV-2 Omicron variant spike glycoprotein (PDB ID: 7WBP).

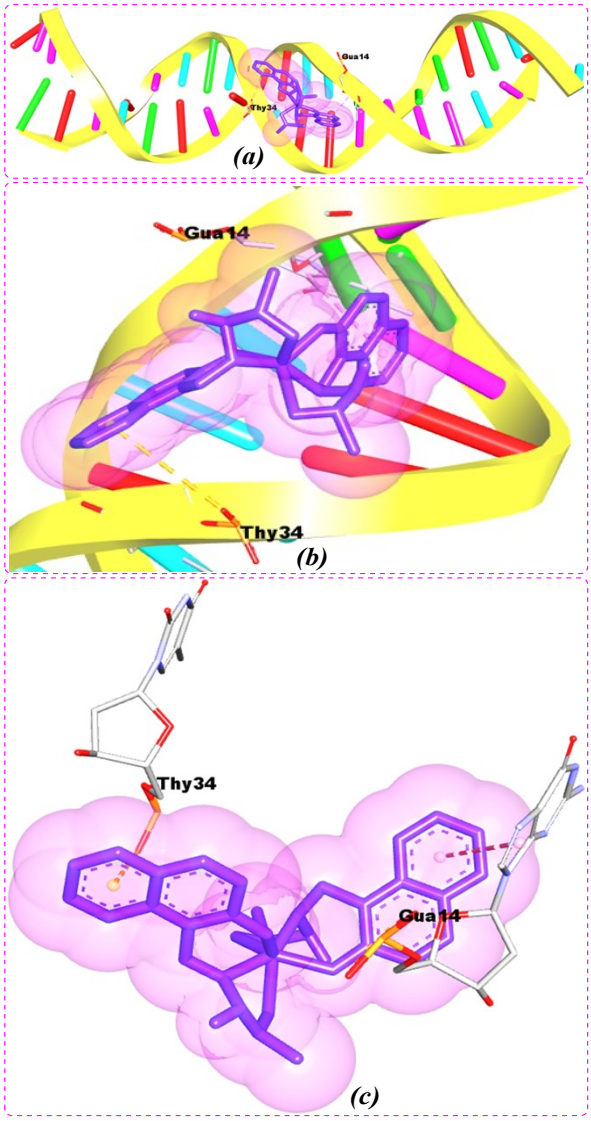

Figure S56. Docked view of Ni(II) complex (**2**) inside the active site of the DNA binding protein (PDB ID: 7UR0) with its focused view for interacting nucleotide residues.

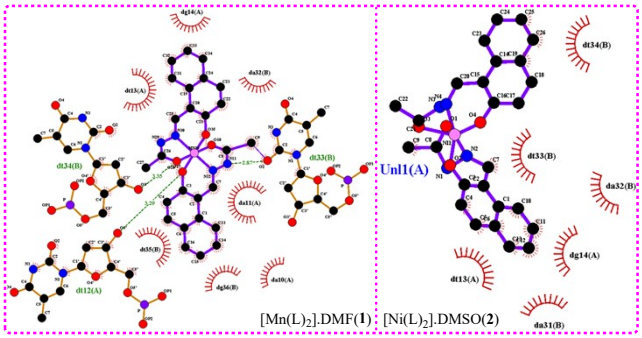

Figure S57. 3D view of the docked Mn(III) complex (**1**) and Ni(II) complex (**2**) with interacting residues inside the active site of the DNA binding protein (PDB ID: 7UR0).

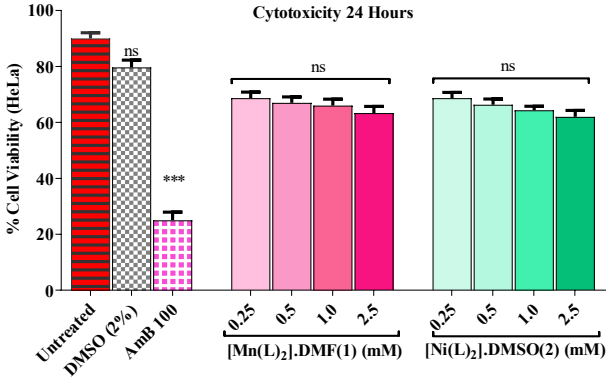

Figure S58. Cell viability on HeLa cell for metal complexes (**1**) and (**2**) after treatment with 24 h.

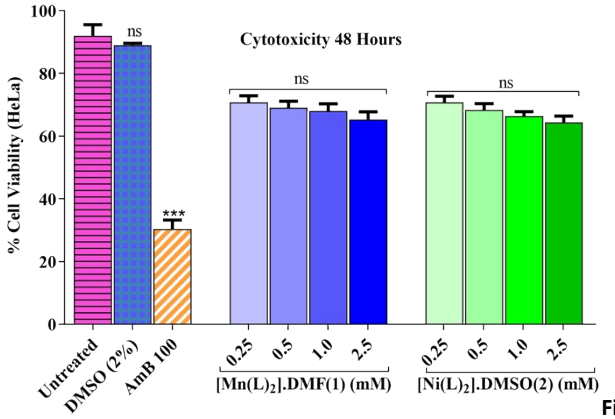

Figure S59. Cell viability on HeLa cell for metal complexes (**1**) and (**2**) after treatment with 48 h.

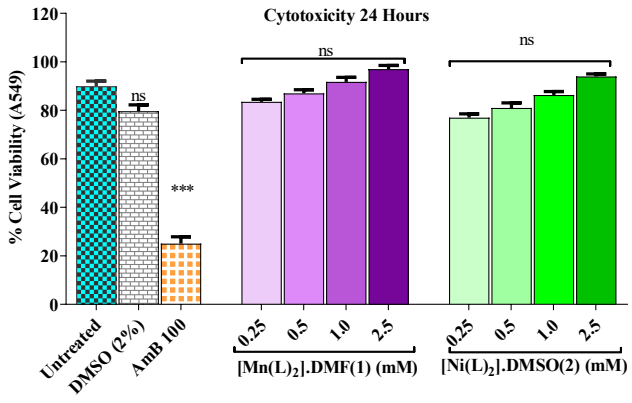

Figure S60. Cell viability on A549 cell for metal complexes (**1**) and (**2**) after treatment with 24 h.

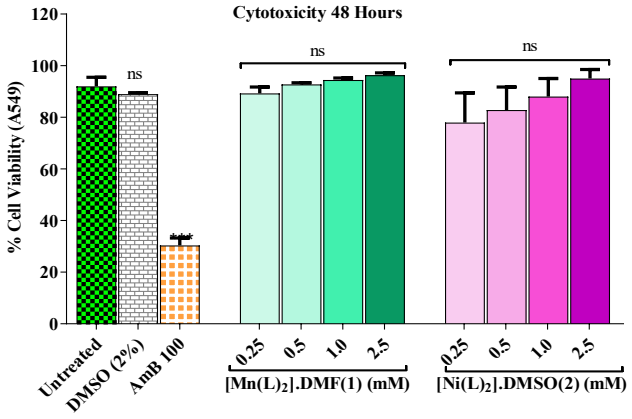

Figure S61. Cell viability on A549 cell for metal complexes (**1**) and (**2**) after treatment with 48 h.

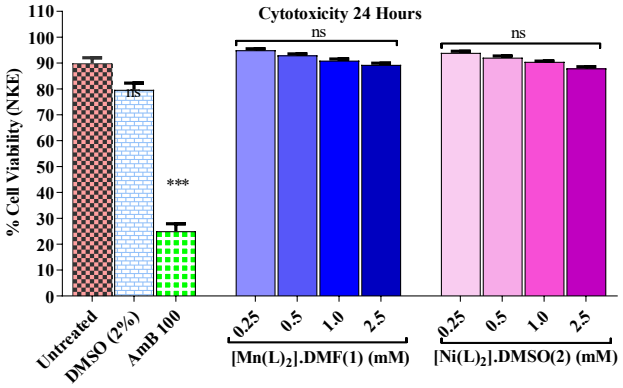

Figure S62. Cell viability on NKE cell for metal complexes (**1**) and (**2**) after treatment with 24 h.

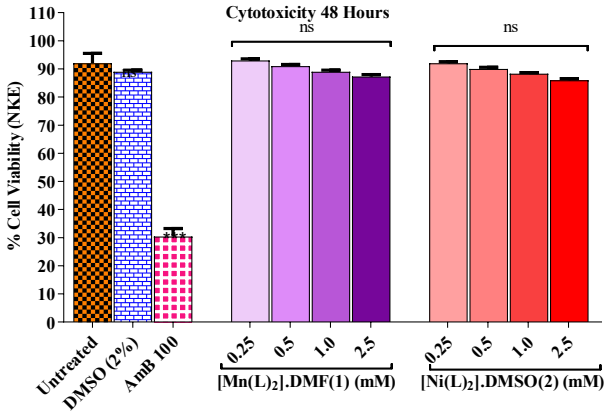

Figure S63. Cell viability on NKE cell for metal complexes (**1**) and (**2**) after treatment with 48 h.

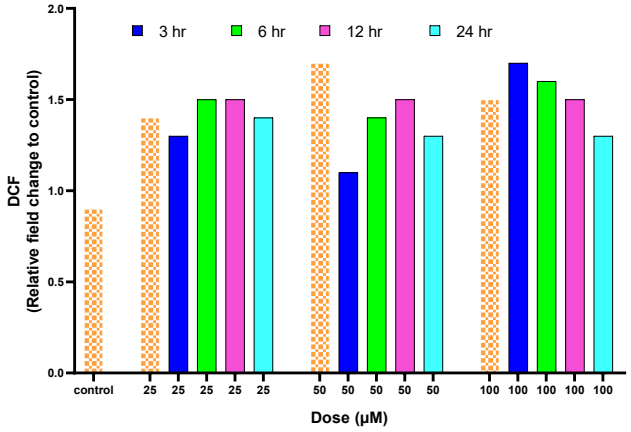

Figure S64. Dose and time-dependent intracellular ROS generation of MCF7 cells treated with the Ni(II) complex (**2**) relative to control, depending on the time of incubation upto 24 h.

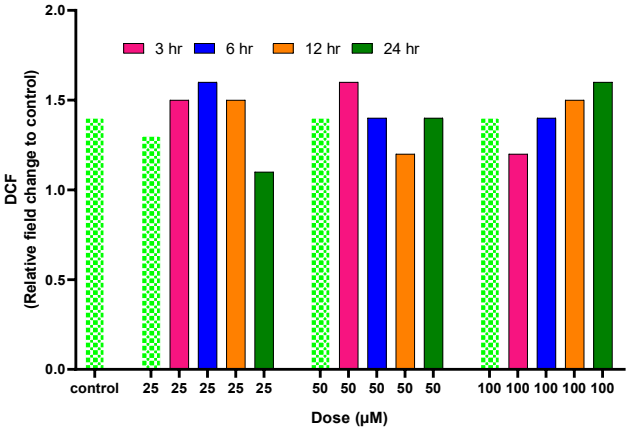

Figure S65. Dose and time-dependent intracellular ROS generation of HeLa cells treated with the Ni(II) complex (**2**) relative to control, depending on the time of incubation upto 24 h.

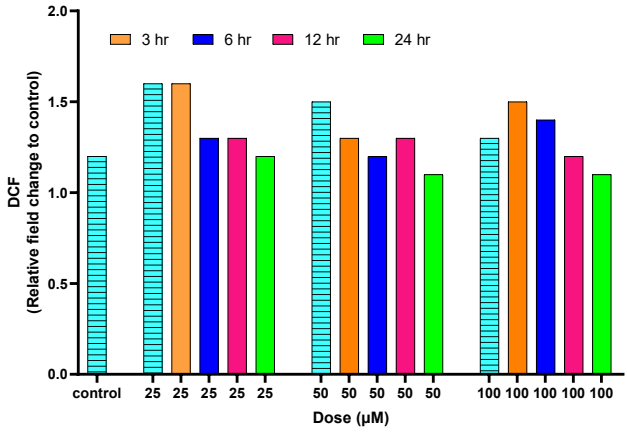

Figure S66. Dose and time-dependent intracellular ROS generation of A549 cells treated with the Ni(II) complex (**2**) relative to control, depending on the time of incubation upto 24 h.

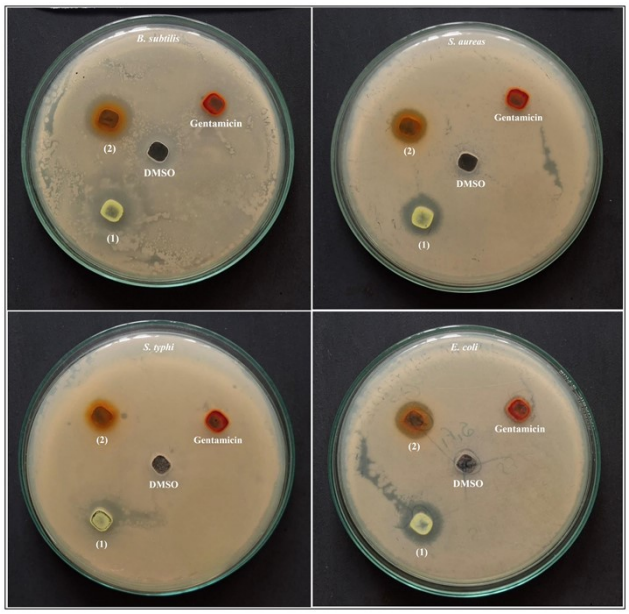

Figure S67. Zone of inhibition from the agar well diffusion test (antibacterial screening activity) of Mn(III) complex (**1**) and Ni(II) complex (**2**) against different species of microorganisms (*Bacillus subtilis, Staphylococcus aureus, Salmonella typhi* and *Escherichia coli*).

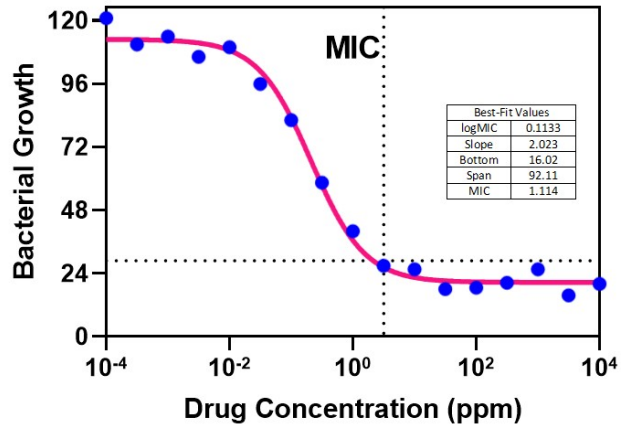

Figure S68. Graphical representation of in-vitro antibacterial activity for Mn(III) complex (**1**) against G(-) bacteria (Escherichia coli) with different drug concentration.

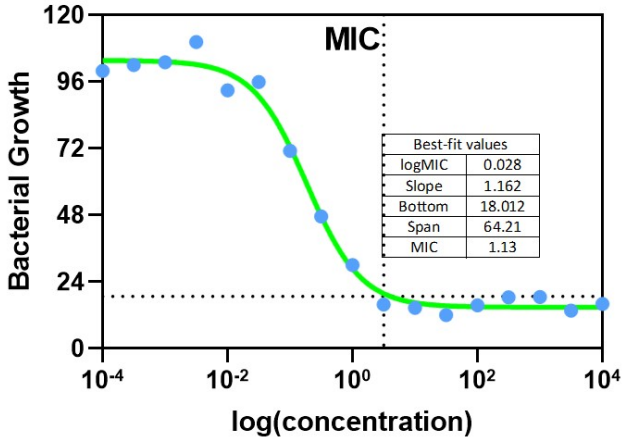

Figure S69. Graphical representation of in-vitro antibacterial activity for Ni(II) complex (**2**) against G(-) bacteria (Escherichia coli) with different drug concentration.

Table S1. Thermal degradation of the complexes (**1**) and (**2**).

Compounds	DSC range (ºC)	Process	ΔH (J/g)	TG-DTG peak(ºC)	Mass loss (%)	Assignments
$[Mn(L)_2]\cdot DMF$(**1**)	228.1	Exo	48.32	225.5 327.7 367.7 447.3 1048.4	-14.19 -17.96 -13.84 -18.69 -11.67	C_3H_7NO C_8H_8 $C_2H_4N_4$ $C_{10}H_4$ C_4H_6 Leaving MnO
$[Ni(L)_2]\cdot DMSO$(**2**)	222.4	Exo	201.9	217.4 378.8 418.2 502.7	-15.14 -26.81 -20.26 -24.37	C_2H_6SO $C_{12}H_8$ $C_{10}H_6$ $C_4H_8N_4O_2$ Leaving NiO

Table S2. A correlation between binding parameters of CT-DNA and BSA with tested complexes (**1**) and (**2**) by using UV-Vis and fluorescence spectral titration.

Compound		k_b (M^{-1})	k_a (M^{-1})	k_q ($M^{-1}s^{-1}$)	n
$[Cu(L)_2]$.DMF(**1**)	DNA	1.07×10^5	5.88×10^5	3.01×10^{11}	0.97
	BSA	1.43×10^5	7.54×10^5	5.06×10^{11}	1.01
$[Ni(L)_2]$.DMSO(**2**)	DNA	1.35×10^5	3.38×10^5	6.25×10^{12}	0.95
	BSA	1.40×10^5	9.54×10^5	2.92×10^{12}	1.05

Table S3. Crystal Data and structure refinement of the metal complexes (**1**) and (**2**).

Crystallographic data	$[Mn(L)_2].DMF$(**1**)	$[Ni(L)_2].DMSO$(**2**)
Empirical Formula	$C_{29}H_{28}MnN_5O_5$	$C_{28}H_{28}N_4NiO_5S$
Mw ($gmol^{-1}$)	581.50	591.31
temp (K)	120(2)	100(2)
λ (Mo Kα), (Å)	0.71073	0.71073
crystal system	Triclinic	Triclinic
space group	P_{-1}	P_{-1}
a (Å)	8.3914(7)	10.6283(7)
b (Å)	11.9823(9)	10.9606(7)
c (Å)	13.8050(12)	12.4775(8)
α (°)	86.538(3)	86.960(2)
β (°)	86.395(3)	87.375(3)
γ (°)	72.921(3)	64.662(2)
V ($Å^3$)	1322.95(19)	1311.43(15)
Z	2	2
D_{calc} (g/cm^3)	1.460	1.497
μ (mm^{-1})	0.549	0.867
F(000)	604	616
Crystal size(mm^3)	0.258 x 0.220 x 0.070	0.210 x 0.110 x 0.052
Theta range for data collection(°)	2.880 to 25.814	2.645 to 25.998
Limiting indices	-10<=h<=10, -14<=k<=14, -16<=l<=16	-13<=h<=13, -13<=k<=13, -15<=l<=15
Reflections collected/ unique	5160 / 5160 [R(int) = 0.0512]	46125/5149 [R(int) = 0.0606]
Completeness to = 25.242	99.5 %	99.8 %
Absorption Correction	Semi-empirical from equivalents	Semi-empirical from equivalents
Max. And min. transmission	0.745262 and 0.547135	0.7458 and 0.5692
Refinement method	Full-matrix -least squares on F^2	Full-matrix least-squares on F^2
Data/restrains/parameters	5160/0/369	5149 / 0 / 364
Goodness-of-fit (GOF) on F^2	1.169	1.033
R_1 [$I > 2\sigma(I)$][a]	R1 = 0.0571, wR2 = 0.1426	R1 = 0.0364, wR2 = 0.0898
wR_2 (all data)[b]	R1 = 0.0663, wR2 = 0.1478	R1 = 0.0402, wR2 = 0.0921
Largest diff. Peak and hole(A^{-3})	0.426 and -0.498	0.634 and -0.610
CCDC Number	2375219	2375220

Table S4. Selected bond lengths (Å) and angles (°) of the metal complexes (**1**) and (**2**).

Complex $[Mn(L)_2].DMF$(**1**)			
Bond lengths (Å)			
Mn(1)-O(3)	1.867(3)	Mn(1)-O(1)	2.046(3)
Mn(1)-O(4)	1.908(3)	Mn(1)-N(1)	2.084(3)
Mn(1)-N(3)	1.959(3)	Mn(1)-O(2)	2.258(3)
Bond angles (°)			
O(3)-Mn(1)-O(4)	169.81(13)	N(3)-Mn(1)-N(1)	165.14(14)
O(3)-Mn(1)-N(3)	89.91(14)	O(1)-Mn(1)-N(1)	83.13(12)
O(4)-Mn(1)-N(3)	79.94(13)	O(3)-Mn(1)-O(2)	89.53(13)
O(3)-Mn(1)-O(1)	93.58(13)	O(4)-Mn(1)-O(2)	89.72(12)
O(4)-Mn(1)-O(1)	91.00(12)	N(3)-Mn(1)-O(2)	91.28(13)
N(3)-Mn(1)-O(1)	111.06(13)	O(1)-Mn(1)-O(2)	157.42(11)
O(3)-Mn(1)-N(1)	93.66(13)	N(1)-Mn(1)-O(2)	74.35(11)
O(4)-Mn(1)-N(1)	95.92(13)		
Complex $[Ni(L)_2].DMSO$(**2**)			
Bond lengths (Å)			
Ni(1)-N(3)	1.9964(17)	Ni(1)-N(2)	1.9998(17)
Ni(1)-O(2)	2.0320(15)	Ni(1)-O(3)	2.0405(15)
Ni(1)-O(4)	2.1119(15)	Ni(1)-O(1)	2.1180(15)
N(1)-N(2)	1.396(2)	N(3)-N(4)	1.392(2)
O(5)-S(1)	1.488(2)		
Bond angles (°)			
N(3)-Ni(1)-N(2)	168.84(7)	N(3)-Ni(1)-O(2)	96.92(6)
N(2)-Ni(1)-O(2)	86.10(6)	N(3)-Ni(1)-O(3)	86.61(6)
N(2)-Ni(1)-O(3)	104.11(6)	O(2)-Ni(1)-O(3)	91.33(6)
N(3)-Ni(1)-O(4)	78.35(6)	N(2)-Ni(1)-O(4)	90.76(6)
O(2)-Ni(1)-O(4)	93.70(6)	O(3)-Ni(1)-O(4)	164.60(6)
N(3)-Ni(1)-O(1)	99.07(6)	N(2)-Ni(1)-O(1)	78.45(6)
O(2)-Ni(1)-O(1)	163.96(6)	O(3)-Ni(1)-O(1)	88.32(6)
O(4)-Ni(1)-O(1)	90.80(6)	S(1)-C(27)-H(27A)	109.5
N(2)-N(1)-H(1N)	119.9(19)	C(3)-N(2)-Ni(1)	129.56(14)
N(1)-N(2)-Ni(1)	112.47(13)	N(4)-N(3)-Ni(1)	112.39(13)
C(2)-O(1)-Ni(1)	111.18(13)	C(5)-O(2)-Ni(1)	128.56(13)
C(14)-O(3)-Ni(1)	129.77(13)	C(25)-O(4)-Ni(1)	111.77(14)

Table S5. Hydrogen bond parameters found in the complexes (**1**) and (**2**).

D-H...A	**D-H (Å)**	**H-A (Å)**	**D-A (Å)**	**D-H-A (°)**
Complex $[Mn(L)_2].DMF$(**1**)				
C(11)-H(11)...O(5)	0.95	2.43	3.229(5)	141.6
C(15)-H(15)...N(4)#1	0.95	2.56	3.509(6)	173.5
C(26)-H(26C)...O(3)#2	0.98	2.56	3.486(5)	157.5
N(2)-H(2N)...O(5)	0.86(5)	1.93(5)	2.764(5)	163(4)
Complex $[Ni(L)_2].DMSO$(**2**)				
C(15)-H(15)...O(5)	0.95	2.45	3.150(3)	130.2
C(26)-H(26A)...O(5)#1	0.98	2.50	3.277(3)	136.4
C(27)-H(27C)...O(4)#2	0.98	2.39	3.224(3)	142.5
N(1)-H(1N)...O(3)#2	0.82(3)	1.89(3)	2.698(2)	168(3)
N(4)-H(4N)...O(2)#3	0.85(3)	1.86(3)	2.698(2)	168(3)

Symmetry transformations used to generate equivalent atoms: #1 x-1,y,z #2 x+1,y,z for complex (**1**); and #1 x,y-1,z #2 -x,-y+1,-z+1 #3 -x+1,-y,-z+1 for complex (**2**)

Table S6. Quantum chemical parameters or global reactivity descriptors (units in eV) as well as FMO energy gap values of the metal complexes (**1**) and (**2**).

Molecular descriptors and energy gap (ΔE_g)	$[Mn(L)_2].DMF$(**1**)	$[Ni(L)_2].DMSO$(**2**)
E_{LUMO}	0.07080	-0.06988
E_{HOMO}	-0.24787	-0.17047
ΔE_g	0.31867	0.10059
$E_{LUMO\ (+1)}$	0.09499	-0.04840
$E_{HOMO\ (-1)}$	-0.27302	-0.17718
ΔE_g	0.36801	0.12878
$E_{LUMO\ (+2)}$	0.11021	-0.04304
$E_{HOMO\ (-2)}$	-0.28941	-0.19899
ΔE_g	0.39962	0.15595
$E_{LUMO\ (+3)}$	0.11685	-0.02664
$E_{HOMO\ (-3)}$	-0.30782	-0.21220
ΔE_g	0.42467	0.18556
Ionization potential, IP = - E_{HOMO}	0.24787	0.17047
electron affinity, EA = -E_{LUMO}	-0.07080	0.06988
electro negativity, χ = (IP + EA)/2	0.0885	0.1201
chemical potential, μ = -(IP + EA)/2	-0.0885	-0.1201
global hardness, η = (IP - EA)/2	0.1593	0.0502
global softness, $\sigma = 1/2\eta$	3.1387	9.9601
Electrophilicity index, $\omega = \mu^2 / 2\eta$	0.0245	0.1436

Energy gap (ΔE) = E_{LUMO}-$E_{HOMO;}$ units in eV

Table S7. Correlations between the experimental geometries of the (**1**) and (**2**) and the theoretical geometries observed upon interactions against SARS-CoV-2 (PDB ID: 8FXC, 6M0J, 8DV1) and Omicron viral RBD proteins (PDB ID: 7TN0 and 7WBP) and DNA (PDB ID: 7UR0).

Docked complexes inside SARS-CoV-2 spike RBD protein, Omicron RBD protein, spike glycoprotein and DNA with bond lengths (Å)	Complexes			
	$[Mn(L)_2].DMF$(**1**)		$[Ni(L)_2].DMSO$(**2**)	
Experimental bond lengths (Å)	Mn(1)-O(1)	2.046(3)	Ni(1)-N(3)	1.9964(17)
	Mn(1)-O(2)	2.258(3)	Ni(1)-O(2)	2.0320(15)
	Mn(1)-O(3)	1.867(3)	Ni(1)-O(4)	2.1119(15)
	Mn(1)-O(4)	1.908(3)	Ni(1)-N(2)	1.9998(17)
	Mn(1)-N(1)	2.084(3)	Ni(1)-O(3)	2.0405(15)
	Mn(1)-N(3)	1.959(3)	Ni(1)-O(1)	2.1180(15)
PDB ID: 8FXC	Mn(1)-O(1)	2.040	Ni(1)-N(3)	1.9950
	Mn(1)-O(2)	2.254	Ni(1)-O(2)	2.0325
	Mn(1)-O(3)	1.869	Ni(1)-O(4)	2.1165
	Mn(1)-O(4)	1.915	Ni(1)-N(2)	1.9942
	Mn(1)-N(1)	2.081	Ni(1)-O(3)	2.0447
	Mn(1)-N(3)	1.954	Ni(1)-O(1)	2.1158
PDB ID: 6M0J	Mn(1)-O(1)	2.041	Ni(1)-N(3)	1.9947
	Mn(1)-O(2)	2.255	Ni(1)-O(2)	2.0358
	Mn(1)-O(3)	1.864	Ni(1)-O(4)	2.1158
	Mn(1)-O(4)	1.906	Ni(1)-N(2)	1.9947
	Mn(1)-N(1)	2.088	Ni(1)-O(3)	2.0482
	Mn(1)-N(3)	1.953	Ni(1)-O(1)	2.1184
PDB ID: 8DV1	Mn(1)-O(1)	2.038	Ni(1)-N(3)	1.9958
	Mn(1)-O(2)	2.251	Ni(1)-O(2)	2.0378
	Mn(1)-O(3)	1.877	Ni(1)-O(4)	2.1148
	Mn(1)-O(4)	1.911	Ni(1)-N(2)	1.9948
	Mn(1)-N(1)	2.072	Ni(1)-O(3)	2.0458
	Mn(1)-N(3)	1.945	Ni(1)-O(1)	2.1151
PDB ID: 7TN0	Mn(1)-O(1)	2.049	Ni(1)-N(3)	1.9991
	Mn(1)-O(2)	2.257	Ni(1)-O(2)	2.0357
	Mn(1)-O(3)	1.861	Ni(1)-O(4)	2.1142
	Mn(1)-O(4)	1.914	Ni(1)-N(2)	1.9984
	Mn(1)-N(1)	2.081	Ni(1)-O(3)	2.0447
	Mn(1)-N(3)	1.951	Ni(1)-O(1)	2.1159
PDB ID: 7WBP	Mn(1)-O(1)	2.045	Ni(1)-N(3)	1.9947
	Mn(1)-O(2)	2.254	Ni(1)-O(2)	2.0374
	Mn(1)-O(3)	1.863	Ni(1)-O(4)	2.1115
	Mn(1)-O(4)	1.914	Ni(1)-N(2)	1.9945
	Mn(1)-N(1)	2.089	Ni(1)-O(3)	2.0454
	Mn(1)-N(3)	1.948	Ni(1)-O(1)	2.1149
PDB ID: 7UR0	Mn(1)-O(1)	2.049	Ni(1)-N(3)	1.9982
	Mn(1)-O(2)	2.252	Ni(1)-O(2)	2.0334
	Mn(1)-O(3)	1.865	Ni(1)-O(4)	2.1102
	Mn(1)-O(4)	1.901	Ni(1)-N(2)	1.9954
	Mn(1)-N(1)	2.086	Ni(1)-O(3)	2.0441
	Mn(1)-N(3)	1.956	Ni(1)-O(1)	2.1164

Table S8. Comparison of binding energies (ΔG) and inhibition / dissociation constants (K_i/K_d) of some metal complexes against SARS-CoV-2 (Omicron) viral proteins obtained from in-silico molecular docking study.

Sl. No.	Complexes	binding energies (kcal/mol)	inhibition/ dissociation constants, [K_i(μM)]	Ref.
1	C1	-10.78	-	24
2	C2	-12.06	-	24
3	C3	-11.24	-	24
4	C1	-5.95	43.22	32
5	C2	-7.43	3.56	32
6	C3	-3.29	210	32
7	C4	-2.99	290	32
8	C5	-7.67	2.38	32
9	$[Mn(H_2L)Cl_2]$	-10.46	-	35
10	$[Ni_3(\mu\text{-}L)_2(bipy)_3]$(**1**)	-8.9	2.373	36
11	$[Ni(L^1)](PPh_3)]DMF$(**1**)	-7.46	3.39	37
12	$[Ni(L^2)]$(**2**)	-7.56	2.89	37
13	$[Cu(L^1)_2]$(**1**)	-9.8	2.912	38
14	$[Cu(L^2)_2]$(**2**)	-9.4	2.813	38
15	$[Cu(L^1)_2]$(**1**)	-9.8	4.253	39
16	$[Cu(L^2)(CH_3OH)(Cl)]$(**2**)	-9.3	3.152	39
17	$[Ni(L)]_2$(**1**)	-11.2	7.134	40
18	$[Ni(L)]_n$(**2**)	-10.5	6.213	40
19	$[Zn(L)(en)]ClO_4$(**1**)	-9.1	2.938	41
20	$[Zn(L)_2]$ (**2**)	-10.2	1.296	41
21	$[Cu(L)_2]$(**1**)	-10.2	2.134	42
22	$[Ni(L)_2]$(**2**)	-9.5	2.203	42
23	$[Mn(L)_2(bpy)]$	-6.9	-	46
24	$[Co(L)_2(bpy)]$	-9.3	-	46
25	$[Ni(L)_2(bpy)]$	-8.2	-	46
26	$[Mn(L)(Phen)_3]^{2+}$	-8.40	0.661	59
27	Nirmatrelvir	-7.89	-	59
28	Ritonavir	-8.63	-	59
29	Remdesivir	-7.70	-	59
30	Lopinavir	-8.21	-	59
31	Favipiravir	-6.71	-	59
32	Hydroxychloroquine	-6.09	-	59
33	Molnupiravir	-8.22	-	59
34	[Cu(L)(phen)](**1**)	-6.18	0.76	60
35	$[Cu(II)(phen)_3]^{+2}$(**1a**)	-8.4	0.661	61
36	$[Ni(L^1)(phen)_2]ClO_4$(**1**)	-11.5	-	62
37	$[Cu(L^2)]$(**2**)	-8.5	-	62
38	$[Mo(dien)O_3]$(**1**)	-9.9	6.539	63
39	$[Cu(phen)_2(Cl)(NCS)]$(**1**)	-7.6	4.567	64
40	$[Ag(pph_3)_3(sal)]$(**1**)	-7.6	4.639	65
41	$[Cu(pph_3)_3Cl]$(**2**)	-8.2	5.742	65
42	$[Mn(L)_2].DMF$(**1**)			This work
	8FXC	-10.5	1.914	
	6M0J	-10.2	2.162	
	8DV1	-11.9	1.369	
	7TN0	-10.2	2.134	
	7WBP	-11.9	1.349	
43	$[Ni(L)_2].DMSO$(**2**)			This work
	8FXC	-10.3	2.157	
	6M0J	-9.5	2.203	
	8DV1	-8.7	2.641	
	7TN0	-9.5	2.231	
	7WBP	-8.7	2.624	

Table S9. IC_{50} values in μM of the metal complexes (**1**) and (**2**) for the antiproliferative activity towards the breast cancer (MCF-7), cervical cancer (HeLa) and lung cancer cell lines (A549) and the results are compared with NKE cell lines after 24 and 48 hr incubation.

Compounds	After 24 hr incubation			
	MCF-7	HeLa	A549	NKE
$[Mn(L)_2].DMF$(**1**)	20.23 ± 0.12	19.34 ± 1.10	25.52 ± 0.11	35.27 ± 1.22
$[Ni(L)_2].DMSO$(**2**)	22.17 ± 0.13	20.65 ± 0.14	27.23 ± 1.26	38.41 ± 1.51
	After 48 hr incubation			

[Mn(L)$_2$].DMF(**1**)	19.54 ± 1.13	18.17 ± 1.65	24.91 ± 1.02	34.62 ± 0.75
[Ni(L)$_2$].DMSO(**2**)	18.61 ± 0.65	19.24 ± 1.12	25.45 ± 0.21	36.43 ± 1.07

Table S10. Antibacterial activity and minimum inhibition concentration values of the metal complexes (**1**) and (**2**) against two G(+) and two G(-) bacteria.

	[Mn(L)$_2$].DMF(**1**)		[Ni(L)$_2$].DMSO(**2**)	
Test Microorganism	Zone of Inhibition	MIC (Minimum inhibitory concentration)	Zone of Inhibition	MIC (Minimum inhibitory concentration)
G (+) bacteria				
Bacillus subtilis	20.2 ± 1.5	1.214	23.5 ± 1.1	1.11
Staphylococcus aureus	19.3 ± 0.9	2.357	17.1 ± 1.1	2.282
G (–) bacteria				
Escherichia coli	20.6 ± 1.1	1.114	20.2 ± 1.2	1.13
Salmonella typhi	17.7 ± 0.6	2.357	15.6 ± 0.7	2.735

Table S11. The Swiss-ADME computed parameters results of the metal complexes (**1**) and (**2**).

Swiss-ADME computed parameter	CQ [a]	HCQ [a]	[Mn(L)$_2$].DMF(**1**)	[Ni(L)$_2$].DMSO(**2**)
M.W (150-500g/mol)	285.43	287.40	511.43	515.19
H-acceptors (≤10)	2	3	4	4
H-donors (≤5)	1	2	2	2
Log P (0.7-5.0)	4.15	3.32	2.37	2.37
No. of violation (Rule of 5)	0	0	1	1
TPSA (20-130 Å^2)	28.16	48.39	85.70	85.70
Rotatable bonds (<9)	7	7	0	0
Log S(>-6)	-3.95	-3.37	-7.65	-7.68
Fraction Csp^3 (>0.25)	0.5	0.47	0.15	0.15

[a] Chloroquine (CQ) and Hydroxychloroquine (HCQ).

Experimental Section

General materials and techniques

Reagents were purchased from commercial sources and used as received. All the solvents used for the synthesis, $Mn(OAc)_3{\cdot}2H_2O$, $Ni(OAc)_2{\cdot}4H_2O$, acetohydrazide and 2-hydroxy-1-naphthaldehyde were obtained from Sigma-Aldrich and were used without further purification. All compounds are >95% pure by HPLC analysis.

Physical measurements

Various elemental analytical data and quantum chemical calculations were used to analyse the newly synthesized metal complexes (**1**) and (**2**) of Schiff base (SB) ligand. Microanalyses were carried out using an Elementar Vario EL III Carlo Erba 1108 elemental analyser. The FT-IR spectra were recorded on a Perkin Elmer system with a FTIR/ATR spectrophotometer in the spectral range 4000-450 cm^{-1} using KBr pellets and the electronic spectra were taken on a Thermo scientific UV-Vis recording spectrophotometer Evolution-3000 in quartz cells. Fluorescence spectra were recorded at room temperature on a Horiba Scientific Fluoromax-4 spectrofluorometer in quartz cells. Melting point was measured on a Boetius micro melting point apparatus. The thermal analysis for both the complexes were investigated by DSC and TG-DTG with NETZSCH STA 449 F3 Jupiter and NETZSCH DSC 204 F1 PHOENIX under nitrogen atmosphere at a heating range of 28-1400°C. NMR spectra were recorded on a Bruker Ultrashield 500 plus 500 MHz FT-NMR Spectrometer. HRMS were measured on a waters XEVO G2-XS QTOF high resolution mass spectrometer.

X-ray Crystallography

The single crystal X-ray diffraction data of the coordination complexes (**1**) and (**2**) were collected at 120(2) and 100(2) K using Bruker D8 VENTURE SC-XRD photon 100 CMOS detector with wavelength switching fully automatic diffractometer, equipped with graphite-crystal incident beam monochromator, and a fine focus sealed tube with Mo-Kα (λ= 0.71073 Å) and the X-ray source at the SAIF, IIT Madras, India. The Bruker SMART software and Bruker SAINT Software were used for data acquisition and data reduction, respectively. The structures were solved by direct methods and refined by full-matrix least-square calculations with the SHELXL-2018/3 software package [1]. All non-hydrogen atoms were refined anisotropically and all hydrogen atoms and carbon were placed in calculated positions, guided by difference maps and refined isotropically. The molecular crystal structures were plotted using ORTEP [2], PLATON [3], Mercury [4], and Olex 2 [5] programs. Complete crystallographic data were deposited at the Cambridge Crystallographic Data Centre, CCDC no. CCDC-2375219 & CCDC-2375220 for the Mn(III) complex (**1**) and Ni(II) complex (**2**), respectively.

Crystal data:

Mn(III) complex [Mn(L)$_2$].DMF(1): Well-shaped light pink block-like crystals of $C_{29}H_{28}MnN_5O_5$, approximate dimensions 0.258 mm x 0.220 mm x 0.070 mm, was used. The integration of the data using a triclinic unit cell yielded a total of 5160 reflections to a maximum θ angle of 25.814° (0.77 Å resolution), of which 5160 were independent reflection (completeness= 99.5 %, R_{int} = 5.12%) and 25.814% were greater than 2σ (F^2). The final cell constants of

a= 8.3914(7) Å, b=11.9823(9) Å, c= 13.8050(12) Å, α= 86.538(3)°, β = 86.395(3)°, γ = 72.921(3)° and V= 1322.95(19) Å^3 are based upon the refinement of the XYZ-centroids of 5160 reflections above 20σ(I) with 2.880°< 2θ< 25.814°. The structure was solved and refined using the space group *P-1*. The final anisotropic full-matrix least-squares refinement on F^2 with 776 variables converged at R_1= 0.0571% for the observed data and wR_2= 0.1478% for all data. The goodness-of-fit was 1.169. The largest peak in the final difference electron density synthesis was 0.426 e$^-$/Å^3, and the largest hole was -0.498e$^-$/Å^3. Based on the final model, the calculated density was 1.460 g/cm^3 and F_{000} 604 e$^-$. The max. and min. transmission were 0.745262 and 0.547135, respectively.

Ni(II) complex [Ni(L)$_2$].DMSO(2): Well-shaped dark green block-like crystals of $C_{28}H_{28}N_4NiO_5S$, approximate dimensions 0.210 mm x 0.110 mm x 0.052 mm, was used. The integration of the data using a triclinic unit cell yielded a total of 46125 reflections to a maximum θ angle of 25.998° (0.77 Å resolution), of which 5149 were independent reflection (completeness= 99.8 %, R_{int} = 6.06%) and 25.998% were greater than 2σ (F^2). The final cell constants of a= 10.6283(7) Å, b= 10.9606(7) Å, c= 12.4775(8) Å, α= 86.960(2)°, β = 87.375(3)°, γ = 64.662(2)° and V= 1311.43(15) Å^3 are based upon the refinement of the XYZ-centroids of 46125 reflections above 20σ (I) with 2.645°< 2θ< 25.998°.The structure was solved and refined using the space group *P-1*. The final anisotropic full-matrix least-squares refinement on F^2 with 776 variables converged at R_1= 0.0364% for the observed data and wR_2= 0.0921% for all data. The goodness-of-fit was 1.033 The largest peak in the final difference electron density synthesis was 0.634 e$^-$/Å^3, and the largest hole was -0.610e$^-$/Å^3. Based on the final model, the calculated density was 1.497 g/cm^3 and F_{000} 616 e$^-$. The maximum and minimum transmission was 0.7458 and 0.5692, respectively.

Hirshfeld surfaces and 2D-fingerprint plots analysis

Hirshfeld surfaces (HSs) and 2D-fingerprint plots (FPs) characteristics of both the complexes (**1**) and (**2**) are analyzed and the intermolecular interactions in the crystal packing are quantified using the crystal explorer 17.5 software [6]. The d_{norm} surfaces are presented as red colour code (shorter than Vander Waals radii), white colour code (equal to Vander Waals radii) and blue colour code (longer than Vander Waals radii). The stabilized contact distance (d_{norm}) was based on d_e vs d_i. It is given by

$$d_{norm} = \frac{d_i - d_i^{vdw}}{r_i^{vdw}} + \frac{d_e - d_e^{vdw}}{r_e^{vdw}} \quad (1)$$

In this function, for each point on Hirshfeld surfaces, two distances are specified, which include d_i and d_e. The d_i and d_e are the distance to the HS from the nearest internal nucleus (inside the HS) and external nucleus (outside the HS), respectively. In the equation (1), r_i^{vdw} and r_e^{vdw} are the Vander Waals radii of the internal and external atoms. The fingerprint plot was used to better understand intermolecular interactions with distances less than the sum of the Vander Waals radii, which were identified by labelling on Figures. Furthermore, the intermolecular interaction energies have been estimated and their topologies explored using energy framework analysis by *Crystal Explorer 17.5* combined with CE-B3LYP/6-31G (d,p) functional/basis set as reported [7,8].

Theoretical details for DFT calculations

The DFT calculations were performed for the newly synthesized complexes (**1**) and (**2**) usig the Gaussian 09 program package [9] and Gaussview 5.09 molecular visualization program [10]. The molecular structure optimization and HOMO-LUMO energies, etc. were studied. The optimization of the geometry was verified by frequency analysis to assure that the structure is at the local minimum on the molecular potential energy surface (PES). It should be noted that the molecular descriptors *viz*. ionization potential (IP), electron affinity (EA), electro negativity (χ), chemical potential (μ), global hardness (η), global softness (σ) and global electrophilicity (ω) of the studied systems, we considered the Koopmans theorem [11] for the DFT calculations.

Protein binding interaction analysis

We further explored the protein binding interaction study of complexes (**1**) and (**2**) with the calf-thymus DNA(CT-DNA) and bovine serum albumin (BSA) using UV-visible and fluorescence spectroscopic methods followed by literature reported [12,13]. The UV-vis absorption titration experiments were performed against a fixed concentration of metal complex and varying the concentration of CT-DNA/BSA. The Wolfe-Shimer equation (eq2) [14,15] was employed to calculate the binding constant (K_b) of the Mn(III) complexes (**1**) and (**2**) with the CT-DNA/BSA.

$$\frac{[DNA]}{(\varepsilon_a - \varepsilon_f)} = \frac{[DNA]}{(\varepsilon_b - \varepsilon_f)} + \frac{1}{K_b(\varepsilon_b - \varepsilon_f)} \quad (2)$$

where [DNA] is the concentration of DNA base pairs, ε_a, ε_f and ε_b correspond to apparent extinction co-efficient for the complex *i.e*. Abs/[complex] in presence of DNA, in absence of DNA and to fully bound DNA respectively. A plot of [DNA]/(ε_a-ε_f) *vs* [DNA] gave a slope and the intercept equal to 1/(ε_b-ε_f) and 1/K_b(ε_b-ε_f), respectively. The binding constant K_b was calculated from the ratio of the slope to the intercept. Furthermore, interaction of complexes (**1**) and (**2**) with CT-DNA and BSA were also investigated using fluorescence spectroscopy. Stern-Volmer plots were obtained and Scatchard analysis was performed using corrected fluorescence data considering the effect of dilution. Linear fit of the data using the Stern-Volmer equation (Eq. 3 and 4) and the Scatchard equation (Eq.5) [16],

$$\frac{F_0}{F} = 1 + K_{sv}[Q] \quad (3)$$

$$K_q = \frac{K_{sv}}{\tau} \quad (4)$$

$$\log\left(\frac{F_0 - F}{F}\right) = logK_a + nlog[Q] \quad (5)$$

where F_0 and F are the emission intensity of CT-DNA/BSA in the absence and in the presence of the quencher(complexes), respectively, [Q] is the concentration, K_{sv} is the Stern-Volmer constant and τ is the average lifetime, gave the fluorescence quenching constant (K_q), the binding constant (K_a) and the number of binding sites (n).

Molecular docking methodologies

Open access docking tools for easy and reproducible docking of metal complexes in the development of new drug candidates are reported in the literature [17]. To explore potential antivirus drug candidates, the antivirus effects of the Mn(III) complex (**1**) and Ni(II) complex (**2**), against the SARS-CoV-2 (PDB ID:8FXC, 6M0J, 8DV1) and the Omicron viral RBD proteins (PDB ID: 7TN0 and 7WBP) were examined. The molecular docking studies were performed using Autodock Tool (ADT) version 1.5.6 software [18]. The receptor binding sites of the SARS-CoV-2 (PDB ID:8FXC, 6M0J and 8DV1) [19-21] and the Omicron viral RBD proteins (PDB ID: 7TN0 and 7WBP) [22,23] were retrieved from the protein data bank and used as receptor proteins. The DNA protein structure (PDB ID: 7UR0) was also obtained from protein data bank and used as receptor protein [24]. Initially, the protein coordinates were prepared by deleting all the water and heteroatoms to make the targeted protein receptor-free. Further, the polar hydrogens and Kollman charges were added to the protein using the *Autodock tool* (ADT) 1.5.6 associated with *Autodock 4.2* software [18]. The prepared protein and ligand (complexes) coordinates are saved in a pdbqt file format using ADT software. The grid box of the desired volume is selected in such a way that the ligand (complex) can rotate freely inside the active site pocket protein. Visualization of docked poses were done by using Discovery studio and Pymol softwares.

Cytotoxicity assay

To explore biological potentials, a superior biological activity was conducted to test the effect of complexes (**1**) and (**2**) on cell viability. Cytotoxicity of the complexes of Schiff base (SB) ligand were investigated on MCF-7 (breast cancer cells), HeLa (cervical cancer cell), A549 (adenocarcinomic human alveolar basal epithelial cells) i.e. lung cancer cells by using the MTT (3-(4, 5-dimethylthiazolyl-2)-2,5-diphenyltetrazolium bromide) assay [25-27] and the results are compared with the normal human kidney epithelial (NKE) cell line. The MCF-7, HeLa, A549 and NKE cells were plated separately in two hundred microliters per well suspension were seeded into 96-well plates at a density of 3×10^3 mL^{-1} and incubated to allow for cell attachment at 37 °C, 5% CO_2, 95% air and 100% relative humidity after 24 hr as well as after 48 hrs. The synthesized complexes (**1**) and (**2**) of concentrations ranging from 0.5-2.0 µM dissolved in DMSO were seeded to the wells. The solutions were incubated at 37 °C for 30 min in dark. The compound stocks were made to ensure that the total DMSO concentration in each well did not exceed 35%. The use of 100 mM amphotericin B (AmB) as a positive control was made under comparable conditions. As negative controls, the untreated PBMCs and 30% DMSO-treated cells were employed.

Cell viability was evaluated by exposing the wells to 40 mL of 0.4 mg mL^{-1} of MTT assay after 24 hours. The wells were given 0.4 mg/mL of MTT and left to incubate for 2 hours at 37 °C after 48 hours. Following the 48-hour treatment period, where six different doses were administered in triplicate. After the microplates were thoroughly mixed, they were allowed to sit on the bench for 20-30 minutes at room temperature for the duration of time. After incubation, a white plate with no transparency was used to transfer 50 µL of the mixture from each well. At a wavelength of 593 nm, the absorbance of the solution was analyzed after shaking the plates for a while. The activity was

expressed in IC_{50}, which requires the compounds to be at a concentration that results in a 50% decrease in absorbance from the control solution. The percentage of growth inhibition of the synthesized complexes (**1**) and (**2**) against 2,2-diphenyl-2-picryl-hydrazyl (DPPH) was determined using the following equation (Eq. 6).

$$\%Growth\ Inhibition = 100 - \frac{Abs(sample)}{Abs(control)} \times 100 \quad (6)$$

where $A_{control}$ is the absorbance of the control, A_{sample} is the absorbance of the test compounds.

A higher absorbance indicates a higher toxicity of the compounds. The relative assay showed that the cells treated with AmB-(100 mM) and Triton-X-100 (1%) as positive controls showed haemolysis as expected ($P < 0.0001$).

In vitro Antibacterial study

The metal-based coordination complexes (**1**) and (**2**) were tested for *in-vitro* antibacterial activity against four microbial strains, including two G (+) bacteria (Bacillus Subtilis and Staphylococcus aureus) and two G (-) bacteria (Escherichia coli, Salmonella typhi). As a first screening, both the complexes (**1**) and (**2**) of Schiff base (SB) ligand were dissolved in DMSO and it was assessed by the agar well diffusion method [28]. The standard antibiotic Gentamicin, along with the metal complexes (**1**) and (**2**), demonstrates a significant reduction in bacterial growth compared to the DMSO solvent control. The inhibition of bacterial growth can be quantitatively assessed by analysing the Gompertz model parameters, particularly the growth rate constant (τ). To evaluate and compare the antibacterial activity of the metal complexes and Gentamicin, the Gompertz model provides valuable insights into the kinetics of bacterial inhibition and the relative efficacy of these antimicrobial agents. As a sigmoidal function, the Gompertz model is typically used to describe microbial growth, and here it is adapted to model the inhibitory effects of the antimicrobial compounds, offering a detailed understanding of their action against the bacteria.

The minimum inhibitory concentration (MIC) values of both the complexes were determined using the broth dilution method to assess their antibacterial activity. Sterile 96-well microtiter plates were used for the experiments, where the tested compounds were serially diluted in DMSO [29] to achieve final concentrations of 10^{-4}, 10^{-2}, 10^{0}, 10^{2}, and 10^{4} ppm. The average MIC values for metal complexes were obtained from triplicate measurements. A second round of testing was performed to confirm the MIC of the active compounds. In these assays, DMSO (30%) was used as a negative control, while gentamicin served as standard antibiotic for antibacterial activity. To evaluate the bacterial inhibition, the growth indicator (G-stain) (100 L of 0.1%) was included in each well. To monitor bacterial growth, a growth indicator (G-stain, 0.1%) was added to each well. All tests were performed in triplicate, and the microplates were incubated at 30°C for up to 48 hours to allow for sufficient bacterial growth.

Prediction of activity spectra for substances (PASS) and pharmacological effects

To estimate the biological activity, particularly antiviral activities, of the studied bioactive phytochemicals, an open source web tool, PASS online (http://www.way2drug. com/) was used[30]. PASS computer programme has the ability to predict 3678 pharmacological effects; mechanisms and special toxicities of the molecule including mutagenicity, carcinogenicity, teratogenicity, and embryotoxicity. Biological activity of the synthesized compounds is predicted by comparing the structure of the compounds with structures of well-known biological active compounds already available in the database. The PASS online database contains over 180000 biologically active compounds and is constantly updated. Furthermore, to establish the probability of the synthesized complexes (**1**) and (**2**) as potential drug candidates, we evaluated the these complexes utilizing the online web tool SwissADME (http://www.swissadme.ch/)[31]. Through this software, we predicted the drug-likeness and pharmacokinetic properties of these compounds based on Lipinski's Rule of Five (Ro5)[32]. SwissADME is an in-depth analytical absorption, distribution, metabolism, excretion and Toxicity (ADMET) software developed to estimate pharmacokinetic and the drug-likeness of compounds. The protocol entails 3D structures upload and generate canonical smiles within the software interface to predict the physicochemical and drug-likeness properties of the complexes.

Synthesis procedures

Synthesis of (E)-N'-((2-hydroxynaphthalen-1-yl) methylene) acetohydrazide (SB)

A tridentate-ONO donor Schiff base (SB) ligand was synthesized as white coloured crystalline products by the refluxing 2-hydroxy-1-naphthaldehyde (20.0 mmol, 3.443 g) with acetohydrazide (20.0 mmol, 1.481 g) in equimolar ratio 1:1 in EtOH for 6 h. The

white coloured crystalline product was obtained, which was filtered, washed with methanol and diethyl ether (2×5 mL), and stored in a desiccator over $CaCl_2$. Colour: white; Yield: 80%; M.p.: > 180°C. ^{1}H-NMR (500 MHz, DMSO d^6): δ 11.25 (1H, s,-OH), δ 9.10 (1H, s, -NH-), δ 8.89 (1H, s, Ar-CH-N-), δ 7.13- 8.48 (6H, m, Ar-H), δ 2.99 (3H, s,-CH_3), ^{13}C {^{1}H} NMR (500 MHz, DMSO d^6): 171.62, 165.86, 158.29, 145.25, 138.63, 132.06, 129.45, 128.25, 123..98, 121.23, 118.53, 110.26, and 21.85 ppm. FT-IR data (KBr/cm^{-1}): 1588 (**ν**C=N), 1280 (**ν**C=S), 3560 (**ν**N-H). UV-Vis **λ** (nm): 311 (in EtOH). Fluorescence data ($\boldsymbol{\lambda}_{nm}$): 320, 350 (EtOH). Elemental analyses: Anal. Calc. for $C_{13}H_{12}N_2O_2$, (%): C, 68.41, H, 5.30; N, 12.27. Found (%): C, 68.39; H, 5.29; N, 12.28. HRMS (m/z): Obs. (calcd) 229.792 (228.25 g mol^{-1}).

***Synthesis of (N'-{[2-(hydroxy)naphthalen-1-yl]methylidene} acetohydra zido) -[N-{[2-(hydroxy)naphthalen-1-yl] methylidene} ethanehydrazonato] -manganese(III) N,N-dimethylformamide solvate,* [Mn(L)$_2$].DMF(1)**

To a DMF solution (10 mL) of $Mn(OAc)_3.2H_2O$ (1 mmol, 0.268 g) was added to a solution of Schiff base (SB) ligand (2.0 mmol, 0.456 g) in DMF (10 mL). The $(C_2H_5)_3N$ as base (3.0 mmol, 40 µL) was added in the reaction mixture. The solution was stirred at 70−80 °C and then subjected to reflux with constant stirring for 5−6 h. The resulting solution was refluxed for 8 h and then left to evaporate slowly at ambient temperature. Well-shaped light pink block-like crystals of the Mn(III) complex (**1**) suitable for single crystal X-ray structure analysis were collected after few days by filtration, washed with MeOH and diethyl ether (2×5 mL) and finally dried at ambient temperature, and store in a desiccator over $CaCl_2$. Yield: 90 %. M.p. 220 °C. FT-IR (KBr/cm^{-1}): 3549 (**ν**N-H), 2927 (**ν**C-H), 1384 (>C=N); 1658 (**ν**ArC=C), 1253 (**ν**C=S), 1087 (**ν**Cu-S), 655 (**ν**Cu-N). UV-Vis **λ** (nm): 321 and 419 (MeOH), 294 and 413 (CH_3CN), 295 and 413 (DMSO) and 295 and 413 (DMF). Fluorescence data ($\boldsymbol{\lambda}_{nm}$): 368 and 451 (MeOH). Elemental analyses: Anal. Calc. for $C_{29}H_{28}MnN_5O_5$, (**1**) (%): C, 59.90; H, 4.85; N, 12.04. Found (%): C, 59.88; H, 4.87; N, 12.03. HRMS (m/z): Obs. (calcd) 582.0019 (581.50 gmol^{-1}). Crystal data: $C_{29}H_{28}MnN_5O_5$, Mw (gmol^{-1}) =581.50, Triclinic, P_{-1}, a= 8.3914(7) Å, b= 11.9823(9) Å, c=13.8050(12) Å, α= 86.538(3)°, β = 86.395(3)°, 1322.95(19)Å^3, µ= 0.549 mm^{-1}, Z = 2, Z'=0.5, T=120(2) K, λ (Mo Kα) = 0.71073 Å, D_{calc} (mg/m^3) =1.460.

***Synthesis of bis(N'-{[2-(hydroxy) naphthalen-1-yl] methylidene} acetohydrazido)-nickel(II)(methanesulfinyl) methane,* [Ni(L)$_2$]. DMSO(2)**

A DMSO solution (10 mL) of Schiff base (SB) ligand (2.0 mmol, 0.456 g) was gradually added to another DMSO solution (10 mL) of $Ni(OAc)_2{\cdot}4H_2O$ (1.0 mmol, 0.248 g). The solution was initially stirred at 80 °C with constant stirring for 5 h. The resulting solution was refluxed for 10 h and then left to evaporate slowly at ambient temperature. Well-shaped dark green block-like crystal of the Ni(II) complex (**2**) suitable for single crystal X-ray structure analysis were collected after few days by filtration, washed with MeOH, and store in a desiccator over $CaCl_2$. Yield: 95 %. M.p. 235 °C. FT-IR (KBr/cm^{-1}): 3502 (**ν**N-H), 2931 (**ν**C-H), 1380 (>C=N); 1658 (**ν**ArC=C), 1258(**ν**C=S), 1091 (**ν**Ni-S), 659(**ν**Ni-N). UV-Vis **λ** (nm): 327 and 418 (MeOH), 320, 360 and 405 (CH_3CN), 322, 369 and 409 (DMSO) and 321, 367 and 408 (DMF). Fluorescence data ($\boldsymbol{\lambda}_{nm}$): 357, 402 and 436 (MeOH). Elemental analyses: Anal. Calc. for $C_{28}H_{28}N_6NiO_2S_2$, (**2**) (%): C, 65.57; H, 4.34; N, 16.10. Found (%): C, 65.54; H, 4.32; N, 16.07. HRMS (m/z): Obs. (calcd) 591.9004 (591.31 gmol^{-1}). Crystal data: $C_{28}H_{28}N_4NiO_5S$, Mw (gmol^{-1}) =591.31, Triclinic, P_{-1}, a= 10.6283(7) Å, b= 10.9606(7) Å, c= 12.4775(8) Å, α= 86.960(2)°, β = 87.375(3)°, γ = 64.662(2)°, V= 1311.43(15) Å^3, µ= 0.867 mm^{-1}, Z = 2, Z'=0.5, T=100(2) K, λ (Mo Kα) =0.71073 Å, D_{calc} (mg/m^3) =1.497.

References

[1]. G. M. Sheldrick, Crystal structure refinement with SHELXL, *Acta Crystallogr. Sect. C: Struct. Chem.*, 2015, **71**, 3-8.

[2]. L. J. Farrugia, *WinGX* and *ORTEP for Windows* : an update, *J. Appl. Crystallogr.*, 2012, **45**, 849-854.

[3]. A. L. Spek, Single-crystal structure validation with the program *PLATON*, *J. Appl. Crystallogr.*, 2003, **36**, 7-13.

[4]. C. F. Macrae, P. R. Edgington, P. McCabe, E. Pidcock, G. P. Shields, R. Taylor, M. Towler and J. Van De Streek, *Mercury* : visualization and analysis of crystal structures, *J. Appl. Crystallogr.*, 2006, **39**, 453-457.

[5]. O. V. Dolomanov, L. J. Bourhis, R. J. Gildea, J. A. K. Howard and H. Puschmann, *OLEX2* : a complete structure solution, refinement and analysis program, *J. Appl. Crystallogr.*, 2009, **42**, 339-341.

[6]. P. R. Spackman, M. J. Turner, J. J. McKinnon, S. K. Wolff, D. J. Grimwood, D. Jayatilaka and M. A. Spackman, *CrystalExplorer* : a program for Hirshfeld surface analysis, visualization and quantitative analysis of molecular crystals, *J. Appl. Crystallogr.*, 2021, **54**, 1006-1011.

[7]. J. J. McKinnon, D. Jayatilaka and M. A. Spackman, Towards quantitative analysis of intermolecular interactions with Hirshfeld surfaces, *Chem. Commun.*, 2007, 3814.

[8]. M. A. Spackman and D. Jayatilaka, Hirshfeld surface analysis, *Cryst. Eng. Comm.*, 2009, **11**, 19-32.

[9]. M. J. Frisch, G. Trucks, H. B. Schlegel, G. E. Scuseria, M. A. Robb, J. Cheeseman, G. Scalmani, V. Barone, B. Mennucci, G. A. Petersson, H. Nakatsuji, M. Caricato, X. Li, H. P. Hratchian, A. F. Izmaylov, J. Bloino, G. Zheng, J. Sonnenberg, M. Hada and D. Fox, Gaussian 09 Revision A.1. Gaussian Inc. Wallingford, CT, 2009.

[10]. R. Dennington, T. Keith and J. Millam, GaussView, Version 5, Semichem Inc., Shawnee Mission, KS, 2009.

[11]. T. Koopmans, Über die Zuordnung von Wellenfunktionen und Eigenwerten zu den Einzelnen Elektronen Eines Atoms, *Physica*, 1934, **1**, 104-113.

[12]. H. Millonig, J. Pous, C. Gouyette, J. A. Subirana and J. L. Campos, The interaction of manganese ions with DNA, *J. Inorg. Biochem.*, 2009, **103**, 876-880.

[13]. R. Raj Kumar, M. K. Mohamed Subarkhan and R. Ramesh, Synthesis and structure of nickel(II) thiocarboxamide complexes: effect of ligand substitutions on DNA/protein binding, antioxidant and cytotoxicity, *RSC Adv.*, 2015, **5**, 46760-46773.

[14]. J. Haribabu, K. Jeyalakshmi, Y. Arun, N. S. P. Bhuvanesh, P. T. Perumal and R. Karvembu, Synthesis, DNA/protein binding, molecular docking, DNA cleavage and in vitro anticancer activity of nickel(II) bis(thiosemicarbazone) complexes, *RSC Adv.*, 2015, **5**, 46031-46049.

[15]. T. Xu, C. Zhang, K. Xia, W. Li, Y. Cao and H. Gu, Small DNAs that Bind Nickel(II) Specifically and Tightly, *Anal. Chem.*, 2021, **93**, 14912-14917.

[16]. R. Khatun, R. Modak, A. S. M. Islam, D. Moni, N. Sepay, R. Mukherjee, G. Das, N. Murmu and M. Ali, Small Molecule Interactions with Biomacromolecules: DNA Binding Interactions of a Manganese(III) Schiff Base Complex with Potential Anticancer Activities, *ACS Appl. Bio Mater.*, 2023, **6**, 3176-3188.

[17]. M. L. A. Hakkennes, F. Buda and S. Bonnet, MetalDock: An Open Access Docking Tool for Easy and Reproducible Docking of Metal Complexes, *J. Chem. Inf. Model.*, 2023, **63**, 7816-7825.

[18]. G. M. Morris, R. Huey, W. Lindstrom, M. F. Sanner, R. K. Belew, D. S. Goodsell and A. J. Olson, AutoDock4 and AutoDockTools4: Automated docking with selective receptor flexibility, *J Comput. Chem.*, 2009, **30**, 2785-2791.

[19]. A. Addetia, L. Piccoli, J. B. Case, Y.-J. Park, M. Beltramello, B. Guarino, H. Dang, G. D. De Melo, D. Pinto, K. Sprouse, S. M. Scheaffer, J. Bassi, C. Silacci-Fregni, F. Muoio, M. Dini, L. Vincenzetti, R. Acosta, D. Johnson, S. Subramanian, C. Saliba, M. Giurdanella, G. Lombardo, G. Leoni, K. Culap, C. McAlister, A. Rajesh, E. Dellota, J. Zhou, N. Farhat, D. Bohan, J. Noack, A. Chen, F. A. Lempp, J. Quispe, L. Kergoat, F. Larrous, E. Cameroni, B. Whitener, O. Giannini, P. Cippà, A. Ceschi, P. Ferrari, A. Franzetti-Pellanda, M. Biggiogero, C. Garzoni, S. Zappi, L. Bernasconi, M. J. Kim, L. E. Rosen, G. Schnell, N. Czudnochowski, F. Benigni, N. Franko, J. K. Logue, C. Yoshiyama, C. Stewart, H. Chu, H. Bourhy, M. A. Schmid, L. A. Purcell, G. Snell, A. Lanzavecchia, M. S. Diamond, D. Corti and D. Veesler, Neutralization, effector function and immune imprinting of Omicron variants, *Nature*, 2023, **621**, 592-601.

[20]. J. Lan, J. Ge, J. Yu, S. Shan, H. Zhou, S. Fan, Q. Zhang, X. Shi, Q. Wang, L. Zhang and X. Wang, Structure of the SARS-CoV-2 spike receptor-binding domain bound to the ACE2 receptor, *Nature*, 2020, **581**, 215-220.

[21]. S. G. Remesh, G. E. Merz, A. F. Brilot, U. S. Chio, A. N. Rizo, T. H. Pospiech, I. Lui, M. T. Laurie, J. Glasgow, C. Q. Le, Y. Zhang, D. Diwanji, E. Hernandez, J. Lopez, H. Mehmood, K. I. Pawar, S. Pourmal, A. M. Smith, F. Zhou, J. DeRisi, T. Kortemme, O. S. Rosenberg, A. Glasgow, K. K. Leung, J. A. Wells and K. A. Verba, Computational pipeline provides mechanistic understanding of Omicron variant of concern neutralizing engineered ACE2 receptor traps, *Structure*, 2023, **31**, 253-264.e6.

[22]. M. McCallum, N. Czudnochowski, L. E. Rosen, S. K. Zepeda, J. E. Bowen, A. C. Walls, K. Hauser, A. Joshi, C. Stewart, J. R. Dillen, A. E. Powell, T. I. Croll, J. Nix, H. W. Virgin, D. Corti, G. Snell and D. Veesler, Structural basis of SARS-CoV-2 Omicron immune evasion and receptor engagement, *Science*, 2022, **375**, 864-868.

[23]. P. Han, L. Li, S. Liu, Q. Wang, D. Zhang, Z. Xu, P. Han, X. Li, Q. Peng, C. Su, B. Huang, D. Li, R. Zhang, M. Tian, L. Fu, Y. Gao, X. Zhao, K. Liu, J. Qi, G. F. Gao and P. Wang, Receptor binding and complex structures of human ACE2 to spike RBD from omicron and delta SARS-CoV-2, *Cell*, 2022, **185**, 630-640.e10.

[24]. A. R. Orun, E. T. Shields, S. Dmytriw, A. Vajapayajula, C. K. Slaughter and C. D. Snow, Modular Protein–DNA Cocrystals as Precise, Programmable Assembly Scaffolds, *ACS Nano*, 2023, **17**, 13110-13120.

[25]. K. I. Ansari, S. Kasiri, J. D. Grant and S. S. Mandal, Apoptosis and anti-tumour activities of manganese(iii)-salen and -salphen complexes, *Dalton Trans.*, 2009, 8525-8531.

[26]. R. Prabaharan, R. Rengan, S. K. Thangavel and J. G. Małecki, Exploration of Antiproliferative Activity and Apoptosis Induction of New Nickel(II) Complexes Encompassing Carbazole Ligands, *ACS Omega*, 2023, **8**, 12584-12591.

[27]. R. Farghadani, J. Rajarajeswaran, N. B. Mohd Hashim, M. A. Abdulla and S. Muniandy, A novel β-diiminato manganese^{III} complex as the promising anticancer agent induces G_0 /G_1 cell cycle arrest and triggers apoptosis via mitochondrial-dependent pathways in MCF-7 and MDA-MB-231 human breast cancer cells, *RSC Adv.*, 2017, **7**, 24387-24398.

[28]. S. Magaldi, S. Mata-Essayag, C. Hartung De Capriles, C. Perez, M. T. Colella, C. Olaizola and Y. Ontiveros, Well diffusion for antifungal susceptibility testing, *Inter. J. Infect. Diseases*, 2004, **8**, 39-45.

[29]. Q.-M. Hasi, Y. Fan, X.-Q. Yao, D.-C. Hu and J.-C. Liu, Synthesis, characterization, antioxidant and antimicrobial activities of a bidentate Schiff base ligand and its metal complexes, *Polyhedron*, 2016, **109**, 75-80.

[30]. P. S., Prediction of activity spectra for substances, *J. Pharmacol. Pharmaco.*, 2011, **2**, 52–53.

[31]. C. A. Lipinski, F. Lombardo, B. W. Dominy and P. J. Feeney, Experimental and computational approaches to estimate solubility and permeability in drug discovery and development settings, *Adv. Drug Deliv. Rev.*, 2012, **64**, 4–17.

[32]. D. Gfeller, A. Grosdidier, M. Wirth, A. Daina, O. Michielin and V. Zoete, SwissTargetPrediction: a web server for target prediction of bioactive small molecules, *Nucleic Acids Res.*, 2014, **42**, W32–W38.